



This is a repository copy of *Comparative study of conventional and unconventional designs of cathode flow fields in PEM fuel cell*.

White Rose Research Online URL for this paper:  
<http://eprints.whiterose.ac.uk/152317/>

Version: Accepted Version

---

**Article:**

Azarafza, A., Ismail, M.S., Rezakazemi, M. et al. (1 more author) (2019) Comparative study of conventional and unconventional designs of cathode flow fields in PEM fuel cell. *Renewable and Sustainable Energy Reviews*, 116. ISSN 1364-0321

<https://doi.org/10.1016/j.rser.2019.109420>

---

Article available under the terms of the CC-BY-NC-ND licence  
(<https://creativecommons.org/licenses/by-nc-nd/4.0/>).

**Reuse**

This article is distributed under the terms of the Creative Commons Attribution-NonCommercial-NoDerivs (CC BY-NC-ND) licence. This licence only allows you to download this work and share it with others as long as you credit the authors, but you can't change the article in any way or use it commercially. More information and the full terms of the licence here: <https://creativecommons.org/licenses/>

**Takedown**

If you consider content in White Rose Research Online to be in breach of UK law, please notify us by emailing [eprints@whiterose.ac.uk](mailto:eprints@whiterose.ac.uk) including the URL of the record and the reason for the withdrawal request.



[eprints@whiterose.ac.uk](mailto:eprints@whiterose.ac.uk)  
<https://eprints.whiterose.ac.uk/>

# **Comparative Study of Conventional and Unconventional Designs of Cathode Flow Fields in PEM Fuel Cell**

Abouzar Azarafza<sup>a,b</sup>, Mohammad S. Ismail<sup>c</sup>, Mashallah Rezakazemi<sup>d,\*</sup>, Mohamed Pourkashanian<sup>c</sup>,

<sup>a</sup> Department of Mechanical Engineering, Curtin University, Perth, Australia

<sup>b</sup> Fluid Research Group and Curtin Institute for Computation, Curtin University, Perth, Australia

<sup>c</sup> Energy 2050, Department of Mechanical Engineering, Faculty of Engineering, University of Sheffield, Sheffield S3 7RD, UK

<sup>d</sup> Faculty of Chemical and Materials Engineering, Shahrood University of Technology, Shahrood, Iran

\* Corresponding author: mashalah.rezakazemi@gmail.com

## **Abstract**

The choice of an appropriate flow field distributor is crucial to circumvent mass and charge transfer resistance-related issues in proton exchange membrane fuel cells (PEMFCs). In this work, incorporating all the anisotropic nature of the gas diffusion layers (GDLs), a three-dimensional, multiphase CFD model is built to perform a comparative study of several types of cathode flow field designs. Three conventional (i.e. parallel, serpentine and interdigitated) and two recently-introduced (i.e. parallel with blocks and the metal foam) flow field designs were considered for the cathode side. The results showed that the best fuel cell performance is obtained with the metal foam flow field as it induces the lowest water saturation, the lowest values and more uniform distribution of current density and temperature as well as relatively medium pressure drop. Compared with the parallel flow field case, the peak power density increases by about 50% when using the metal foam flow field and by about 10% when using the other three investigated flow fields (i.e. serpentine, interdigitated and parallel with blocks). The parametric analysis reveals that the metal foam outperforms other designs at intermediate and high humidity conditions whereas the interdigitated flow field design outperforms other designs at low humidity conditions.

**Keywords:** PEM fuel cell; flow field design; global and local performances, comparative and parametric analyses, metal foam, partially blocked channels

## **1. Introduction**

Over the last two decades, proton exchange membrane fuel cells (PEMFCs) technology has received a good deal of attention as a promising replacement for the conventional power conversion technologies. Appealing features such as high efficiency, low operating temperature ( $<100\text{ }^{\circ}\text{C}$ ), simple design and, most importantly, having zero/low emission, have all made PEMFC technology a viable source of power for a multitude of mobile auxiliary applications, Combined Heat and Power (CHP), automotive and stationary devices. Despite the significant progress over the last years, high cost of some fuel cell components, relatively low durability and technical issues associated with storing of hydrogen and managing heat and water have all hampered the widespread commercialization of PEMFCs [1,2]. Heat and water management are two critical issues that play a major role in the efficient operation of a PEMFC system. Efficient water management must be ensured especially at low operating voltages where the accumulated water significantly impacts the normal operation of the fuel cell by obstructing CLs/GDLs pores at the cathode, hindering the supply of oxygen to the reactive sites, causing a sharp decline in the cell performance [3,4]. Thermal management is another important issue of PEM fuel cell performance, and it should be considered along with water management. This is highlighted when we note that most physical parameters in fuel cells such as kinetic parameters, water activity, species diffusivities, heat capacities, and saturation pressure are influenced by temperature changes in fuel cells [5]. Of the practical strategies to address the problem, is through the efficient design of flow field plates, especially at the cathode side where water and heat effects are significantly higher than those at the anode side [6]. The efficient design of flow field has shown to be a practical way to alleviate the aforementioned issues by rendering a more uniform distribution of reactants, which in turn, results in better distribution of current densities and heat and water throughout the cell [7,8]. Flow fields designed appropriately must

ideally distribute the reacting gases evenly to the reactive sites in the CLs, and equally, maintain the pressure drop along the flow channels to a minimum. An optimally-designed flow field may enhance the fuel cell performance up to 50% [7,9].

There have been several thorough reviews on conventional and non-conventional designs of the flow field in the literature [9,10]. Wang [10] stated that the “uneven flow distribution” is the main root of all the challenges that hampers the scale-up and commercialization of PEMFCs technology. Optimal design of flow field circumvents the gas mal-distribution in the GDLs and CLs and ensures heat and water balance inside the fuel cells [11]. This is however, a challenging task due to the presence of several conflicting factors that need to be carefully and simultaneously taken into consideration. A look at the literature reveals that there have been plenty of experimental and numerical investigations with the aim of developing more efficient flow field designs for fuel cells. A good number of these studies have been carried out on the most commonly-used flow field designs, i.e., straight channel, serpentine and interdigitated. In these studies, researchers investigated different aspects of the flow fields design in the conventional layouts: flow channel geometry and aspect ratios [12,13], size and number of channels [14], various flow configurations (single and multiple flow pattern) [15,16], the impact of operational parameters [17].

On the other hand, studies have been conducted to develop novel flow fields, either inspired by nature [18,19]; developed with new structures such as metal sheets [20,21] and porous metal foams [6,22,23]; or proposed by various blockage arrangements of parallel flow channel [24–26]. Tseng et al. [22,27] experimentally showed that both low-temperature and high-temperature PEM fuel cells perform better with metal foam flow field. Carton et al. [28] concluded that fuel cell performs better with the open cellular foam than with the conventional flow field designs. Yuan et al. [29] reviewed the use of

porous metal materials as a flow field, current collector, GDL and CL in PEMFC. Afshari et al. [30,31] numerically explored the feasibility of using metal foams as a coolant flow distributor and membrane humidifier in PEMFCs. Placing blocks within flow fields has experimentally and numerically shown to improve the mass transfer of the reactive gases and, accordingly, the overall cell performance [6,25]. Tiss et al. [26] studied the impact of the tilt angle of partial blocks present in the flow channels and found out that it significantly impacts the cell performance, especially at low operating voltages. Heidary et al. [25] built a multiphase PEMFC model to compare in-line and staggered blocks at the cathode flow channels. The results showed that flow channels with staggered blocks enhance the cell performance by 7% compared with the in-line blocks. Afshari et al. [6] developed a single-phase PEMFC model for a single channel and investigated the feasibility of using two recently-focused designs of the cathode flow fields, namely porous-based metal foam and parallel flow field with partially-restricted baffles.

An efficiently-designed flow field, especially at the cathode, has been demonstrated to be a practical solution to mitigate the undesirable issues associated with heat and water management in the PEMFCs. Despite significant experimental and numerical attempts that have been devoted to devising more efficient cathode flow fields, these studies are still sparse. Due to the difficulties in conducting experiments, numerical tools play a significant role to help researchers by offsetting time and cost imposed by trial and error. However, imposing oversimplifying assumptions such as single phase flow model, homogenous GDL, isothermal conditions, etc. especially for the cathode side where water appears as both vapor and liquid, make the capabilities of these models for real PEMFC systems equivocal [6,22]. This is inconsistent with the fact that the existence of liquid water, especially at the cathode, significantly impacts the cell performance and should be taken into account in PEM fuel cell models, at least, at medium and low operating

voltages. Besides, in most of these studies, the suggested models have been solely applied for a specific type of flow field (i.e. usually parallel with the single channel). This can be especially generalized to some recently-introduced flow fields such as metal foam and those with embedded blocks that have been suggested as promising alternatives for conventional designs. Also, the anisotropic nature of the GDLs, which has been shown to have a significant impact on water and thermal management in PEMFC, has not been considered in these models [5,32]. Even with the novel designs, some key questions remain unanswered:

- 1) Under realistic conditions, which PEMFC flow field design, conventional or unconventional, performs better in terms of overall performance and the uniformity of the distribution of the key variables such as the concentration of the reactant gas, temperature and water saturation?
- 2) Upon addressing the above question, the second question that follows is that, for each flow field design, how sensitive the fuel cell performance is to the changes in the operating conditions, i.e. the inlet temperature, humidity and stoichiometric ratio?

Therefore, the main objective of this work is to address the above two questions and acquire valuable knowledge that is of great interest to designers of PEMFCs in industry and academia. Apart from carrying out a detailed multiphase, non-isothermal model with all GDL anisotropic features taken into account, we conduct some parametric analysis and compared the results of the aforementioned layouts at different operating conditions of the fuel cell. Up to the best of authors' knowledge, such a comprehensive comparative study, with a comprehensive 3D numerical model, has not been previously undertaken.

To this end, we establish a detailed 3D, multiphase, non-isothermal CFD model, which also includes anisotropic nature of GDLs, to comparatively study the impacts of various

flow field designs on the PEM fuel cell performance and local transport phenomena. Also, we conduct parametric studies to investigate the impact of relative humidity, inflow temperature and stoichiometric flow ratio on the performance of the modeled fuel cell. To achieve all the above goals, we modeled and compared the results of three commonly-used conventional (i.e. single parallel, single serpentine and interdigitated) and two unconventional (i.e. porous metal foam and parallel with partially staggered blocks) flow field designs which were shown to have good performance as evidenced from the findings reported in the References [ADD REFERENCES].

## **2. Model development**

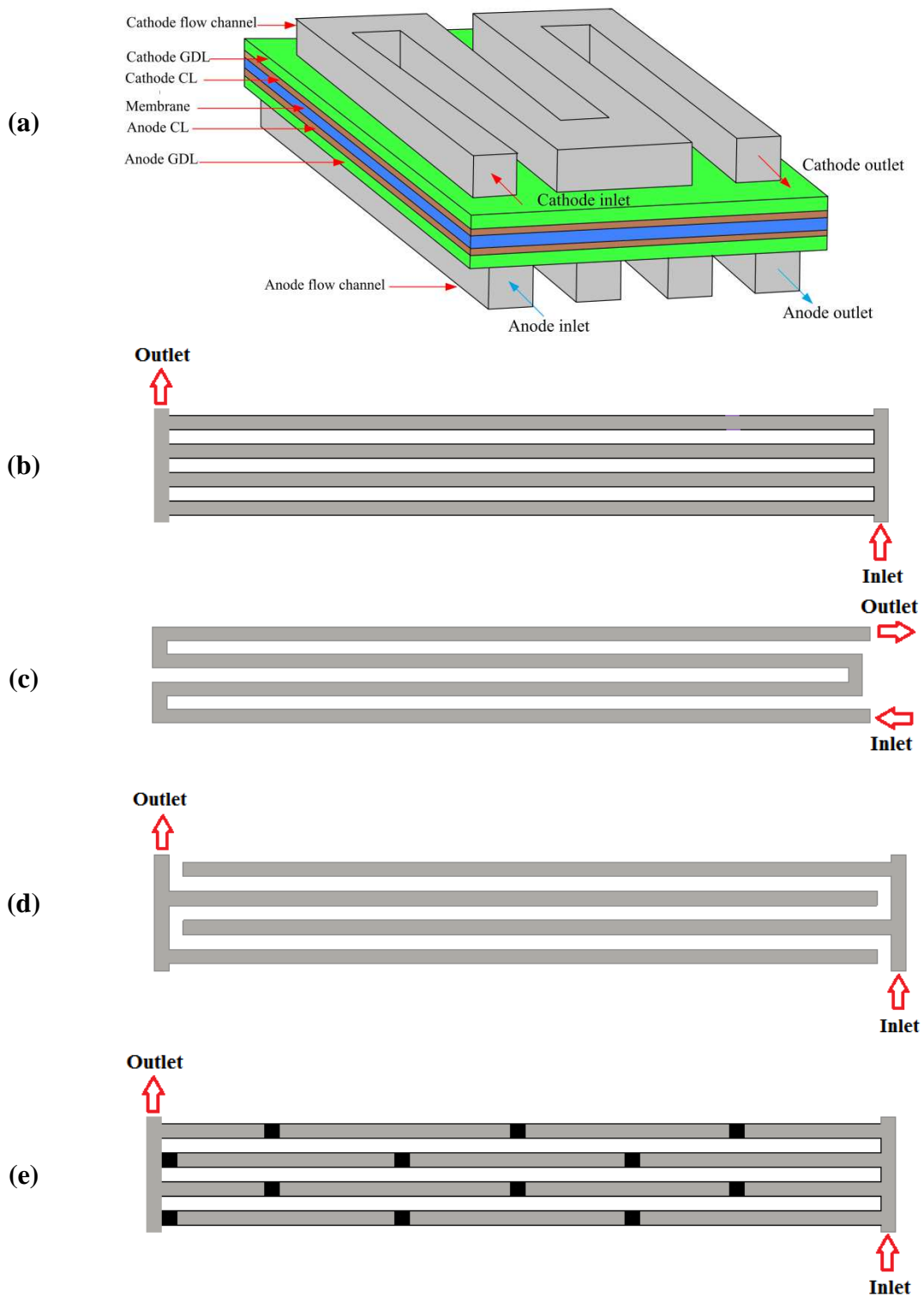
Without compromising the purpose of the study, the following assumptions were made to save computation time:

1. The PEMFC operates under steady-state condition.
2. The gas mixture is assumed as ideal and incompressible.
3. The flow in the flow channels is laminar.
4. The flow in the channels is of mist form and therefore no liquid water exists in the flow channels (however, depending on the water activity, liquid water could exist in the GDLs and the CLs).
5. The physical properties of the catalyst layers and the membrane are assumed to be homogenous and isotropic.

### **2.1. Computational domains**

To save computational time, we only modeled a part of the fuel cell for all the case studies which is equivalent to 4 parallel flow channels. The computational domain for each case consists of 7 components: 2 GDLs, 2 catalyst layers, 2 flow channels, and a single polymeric membrane. Fig. 1 shows different flow fields layouts considered for the present work, namely straight parallel, serpentine and interdigitated flow field as conventional

layouts and metal foam and partially blockage channels as non-conventional layouts. A typical computational domain with a serpentine flow field at the cathode side used for developing CFD model aslo depicted in Fig. 1.



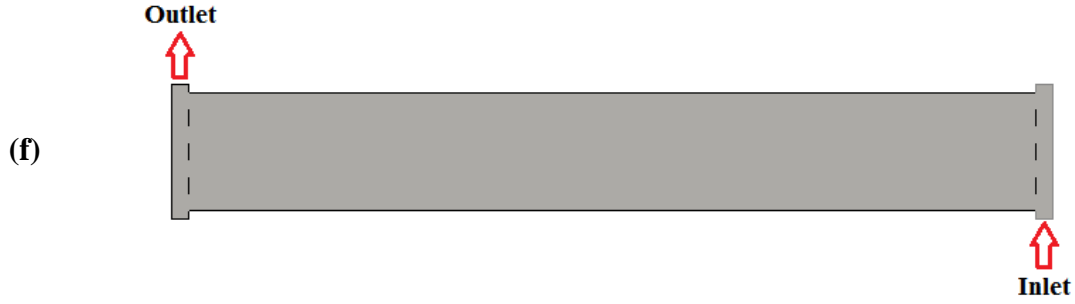


Fig. 1. (a) The computational domain for the serpentine PEMFC used and schematic diagrams for the flow field layouts used at the cathode side of the PEMFC model: (b) single-parallel, (c) single-serpentine, (d) interdigitated, (e) parallel with blocks and (f) metal-foam flow field.

Table 1. lists all the dimensions and operating conditions used in this study and Table 2 lists all the parameters used for developing the the model.

**Table 1**

The dimensions of the PEMFC and the operating conditions used in the present work.

Parameter	Unit	Value	Reference
Channel length	mm	50	[5]
Channel width	mm	1	[5]
Channel height	mm	1	[5]
Rib width	mm	1	[5]
Membrane thickness	mm	0.23	[33]
Gas diffusion layer thickness	mm	0.26	[33]
Catalyst layer thickness	mm	0.0287	[33]
Blockage length/height	mm	1/0.8	[25]
Anode pressure	atm	3	[34]
Cathode pressure	atm	3	[34]
Inlet fuel and air channels temperature	K	353	[34]
Relative humidity of fuel and air channel inlets	%	100/100	[34]
Inlets stoichiometric flow ratio anode/cathode	-	3/3	[34]

**Table 2**

The parameters used for the PEMFC model.

Parameter	Unit	Value	Reference
<b>Kinematic parameters</b>			
Anode reference current density, $j_a^{Ref}$	A m <sup>-3</sup>	$1.4 \times 10^{11}$	[34]
Cathode reference current density, $j_c^{Ref}$	A m <sup>-3</sup>	10	[34]
Anode charge transfer coefficient, $\alpha_a$	-	2	[33]
Cathode charge transfer coefficient, $\alpha_c$	-	2	[33]
Anode reference concentration, $C_{H_2}$	k mol m <sup>-3</sup>	0.0564	[34]
Cathode reference concentration, $C_{O_2}$	k mol m <sup>-3</sup>	0.00339	[34]

Anode concentration exponent	reference -	0.5	[34]
Cathode concentration exponent	reference -	1	[34]
<b>Membrane</b>			
Thermal conductivity	W m <sup>-1</sup> .K <sup>-1</sup>	0.29	[35]
Equivalent weight	kg Kmol <sup>-1</sup>	1100	
Permeability	m <sup>2</sup>	10 <sup>-12</sup>	[31]
Porosity		0.5	[31]
<b>Gas Diffusion Layer</b>			
Electrical conductivity (In-plane/Through-plane)	S m <sup>-1</sup>	5000/500	[36]
Thermal conductivity (In-plane/Through-plane)	W m <sup>-1</sup> .K <sup>-1</sup>	21/1.7	[32]
Porosity		0.6	[37]
Pore blockage saturation exponent		2.0	[25]
Water contact angle		110	[32]
<b>Catalyst Layer</b>			
Electrical conductivity		300	[38]
Thermal conductivity	W m <sup>-1</sup> K <sup>-1</sup>	0.27	[35]
Permeability	m <sup>2</sup>	1.00 × 10 <sup>-13</sup>	[35]
Porosity		0.3	[37]
<b>Porous metal foam (Nickel)</b>			
Permeability	m <sup>2</sup>	10 <sup>-8</sup>	[31]
Thermal conductivity	W m <sup>-1</sup> K <sup>-1</sup>	447	[6]
Porosity	-	0.9	[31]

## 2.2. Governing equations

A 3-dimensional, steady-state and multiphase model has been developed here. It accounts for a set of non-linear, partial differential equations representing the underlying mass, momentum, species, electronic charge, protonic charge, energy, dissolved water, and liquid water transport equations which are all coupled with electrochemical reactions. The following is the description of the governing equations.

### 2.2.1. Conservation of mass and momentum

The conservation equations of mass and momentum in the gas phase are as follows [5]:

$$\nabla \cdot (\rho_g \vec{u}_g) = S_u \quad (1)$$

$$\nabla \cdot \left( \frac{1}{(\varepsilon^{\text{eff}})^2} \rho_g \vec{u}_g \vec{u}_g \right) = -\nabla p_g + \nabla \cdot \left( \frac{1}{\varepsilon^{\text{eff}}} \mu_g \nabla \vec{u}_g \right) + S_m \quad (2)$$

where  $\varepsilon^{\text{eff}}$  is the effective porosity of different components of the fuel cell and is related to the bulk porosity and the liquid saturation,  $\varepsilon^{\text{eff}} = \varepsilon(1-s)$ . Also,  $\vec{u}_g$  and  $\mu_g$  are the velocity vector and the viscosity of the gaseous phase mixture, respectively.

### 2.2.2. Conservation of species transport

The general transport equation of the gas species involved in the PEMFC model is described as [5]:

$$\nabla \cdot (\rho_g \vec{u}_g \omega_i) = \nabla \cdot (\rho_g D_i^{\text{eff}} \nabla \omega_i) + S_i \quad (3)$$

where  $\omega_i$  denotes the mass fraction of each species  $i$ , i.e., hydrogen, oxygen, water vapor, and nitrogen;  $D_i^{\text{eff}}$  is the effective diffusivity of the species  $i$  in the porous media [39]:

$$D_i^{\text{eff}} = f(\varepsilon)g(s)D_i \quad (4)$$

where  $D_i$  is the molecular diffusivity of the species, which is related to the temperature and pressure:

$$D_i = D_i^{\text{ref}} \left( \frac{T}{T_{\text{ref}}} \right)^{3/2} \left( \frac{P_{\text{ref}}}{P} \right) \quad (5)$$

Where  $g(s)$  is a function used to account for the liquid water saturation,  $D_i^{\text{ref}}$  is the mass diffusivity of the species at the reference temperature and pressure. The term  $f(\varepsilon)$  is described by Tomadakis and Sotirchos [40] model based on the percolation theory for a random fibrous porous medium:

$$f(\varepsilon) = \varepsilon \left( \frac{\varepsilon - \varepsilon_p}{1 - \varepsilon_p} \right)^\alpha \quad (6)$$

where  $\varepsilon_p$  is the percolation threshold, equal to 0.11 and  $\alpha$  is the empirical constant, which differs for the in-plane and through-plane directions. The value of  $\alpha$  is 0.521 and 0.785, for the in-plane and through-plane, respectively. The term  $g(s)$  is used to take water saturation into account represented by  $(1-s)^n$  and  $n$  is multiphase saturation exponent for

pore blockage, which was experimentally determined as 2 [28,41]. Note that, apart from the metal foam case where the porosity of the flow channels is specified as 0.8, the porosity is assumed to be 1 for the flow channels in all the cases.

In the CLs, as the pore size is comparable to the mean free path of the gas, Knudsen diffusion is taken into account to address the wall-molecules interactions. Hence, the effective diffusivity for the CLs is rewritten as:

$$D_i^{\text{eff}} = (1-s)^n \varepsilon^{1.5} \left( \frac{1}{D_i} + \frac{1}{D_i^k} \right)^{-1} \quad (7)$$

where  $D_i^k$  is the Knudsen diffusivity and can be calculated from the kinetic theory of gases:

$$D_i^k = \frac{2}{3} \left( \frac{8RT}{\pi M_i} \right)^{0.5} r_p \quad (8)$$

where  $r_p$  denotes the characteristic pore length of the catalyst particles,  $M_i$  is the molecular weight of the species  $i$  in the gas mixture,  $T$  is temperature, and  $R$  is universal gas constant (8.314 J/mol.K).

### 2.2.3. Conservation of electrical charges

The main driving force of the reactions in the fuel cell is the overpotential at the surface of catalyst layers, which is described as the difference between the solid-phase potential and the membrane phase potential. Hence, two transport equations must be solved for: one for the transport of electrons through the solid phase and another for the transport of protons through the electrolyte (or membrane) phase [5]:

$$\nabla \cdot (\sigma_s^{\text{eff}} \nabla \phi_s) + S_{\phi_s} = 0 \quad (9)$$

$$\nabla \cdot (\sigma_m^{\text{eff}} \nabla \phi_m) + S_{\phi_m} = 0 \quad (10)$$

where  $\phi_s$  and  $\phi_m$  represent the electrical and protonic potentials of the solid and electrolyte phases, and  $\sigma_s^{eff}$  and  $\sigma_m^{eff}$  are their corresponding effective values, respectively.

The  $S_{\phi_s}$  and  $S_{\phi_m}$  are related to the electrochemical reactions, namely hydrogen oxidation reaction (HOR) at the anode electrode and oxygen reduction reaction (ORR) at the cathode electrode through Butler-Volmer equation [6]:

$$j_a = (1-s) \left( \xi_a j_a^{ref} \right) \left( \frac{C_{H_2}}{C_{H_2}^{ref}} \right)^{0.5} \left[ \exp\left( \frac{\alpha_{a,a} F}{RT} \eta_{act,a} \right) - \exp\left( -\frac{\alpha_{a,c} F}{RT} \eta_{act,a} \right) \right] \quad (11)$$

$$j_c = (1-s) \left( \xi_c j_c^{ref} \right) \left( \frac{C_{O_2}}{C_{O_2}^{ref}} \right) \left[ \exp\left( \frac{\alpha_{c,a} F}{RT} \eta_{act,c} \right) - \exp\left( -\frac{\alpha_{c,c} F}{RT} \eta_{act,c} \right) \right] \quad (12)$$

where  $j_a$  and  $j_c$  are the current density at anode and cathode respectively,  $j_a^{ref}$  and  $j_c^{ref}$  are the exchange current densities at reference temperature of 25°C and pressure of 1 atm, and  $\alpha_{a,\alpha}$  and  $\alpha_{a,c}$  represent the anode and cathode transfer coefficients of the reaction at the anode, respectively. Similarly,  $\alpha_{c,\alpha}$  and  $\alpha_{c,c}$  are the anode and cathode transfer coefficients of the reaction at the cathode electrode, respectively.  $C_{H_2}$  and  $C_{O_2}$  are the hydrogen and oxygen molar concentrations at the anode and cathode electrodes, respectively and  $C_{H_2}^{ref}$  and  $C_{O_2}^{ref}$  are the hydrogen and oxygen concentration at reference temperature and pressure, and  $\xi_a$  and  $\xi_c$  are the specific active surface area of the anode and cathode CLs (1/m), defined as [43]:

$$\xi = \frac{\text{Catalyst loading} \times \text{Surface area}}{\text{Thickness of catalyst layer}} \quad (13)$$

where the values for the catalyst loading, surface area and catalyst thickness for the anode and cathode CLs used in the present work collected from the literature [34]. The local surface overpotentials,  $\eta_{act}$ , at the anode and cathode electrodes are expressed as follows:

$$\text{HOR at the anode CL:} \quad \eta_{act} = \phi_s - \phi_m \quad (14)$$

ORR at the cathode CL: 
$$\eta_{\text{act}} = \phi_s - \phi_m - U_o \quad (15)$$

where  $U_o$  is the equilibrium (or thermodynamic) potential. At the anode terminal, this value is zero, whereas at the cathode terminal, it is given by Nernst Equation [44]:

$$U_o = 1.482 - 0.000845T + 0.000043T \ln \left( P_{H_2} P_{O_2}^{0.5} \right) \quad (16)$$

where  $T(K)$  is temperature and  $P_{H_2}$  and  $P_{O_2}$  are the partial pressures of hydrogen and oxygen gases which could be calculated using the ideal gas law:  $P_i = y_i * C * R * T$ , where  $y_i$  is the mole fraction of species  $i$  (hydrogen or oxygen) and  $C$  is total molar concentration of the mixture at either side of the fuel cell.

Note that the partial pressure of water was not included in Equation (16) as the water activity of water vapour is normally assumed to be 1 in the molecular region of the water-generating electrode. This is a valid assumption as water generation is always at the catalyst surface and the reaction is not limited by the concentration of product water at this surface [Ref.: Fuel Cell Engines by M.M. Mench].

In the GDLs, electrical conductivity shows strongly anisotropic characteristics and thus has different values for the electrical conductivity in the in-plane and through-plane directions; the anisotropic values are given in Table 2. The proton (electrolyte) conductivity,  $\sigma_m$ , increases with temperature and water content as shown in the following empirical formula [39]:

$$\sigma_m = (0.5139\lambda - 0.326) \exp \left[ 1268 \left( \frac{1}{303} - \frac{1}{T} \right) \right] \quad (17)$$

where  $\lambda$  denotes the membrane water content.

#### 2.2.4. Transport of dissolved water

Dissolved water occurs in the membrane and the CLs. As the operating pressures of the cathode and anode sides for the modeled fuel cell are equal in this paper, the hydraulic permeation effects are deemed to be negligible. Consequently, the governing equation for the transport of dissolved water is described as follows [45]:

$$\nabla \cdot \left( -\frac{n_d}{F} \sigma_1 \nabla \phi \right) = \nabla \cdot \left( D_w^m \frac{\rho_{Naf}}{EW} \nabla \lambda \right) + S_\lambda \quad (18)$$

The left term in Eq. (18) represents the electro-osmotic drag (EOD) of dissolved water and the first term at the right-hand side of the equation represents the back diffusion of the dissolved water.  $n_d$  is the electro-osmotic drag coefficient; it indicates the number of the water molecules carried by each proton from anode to cathode defined as [39]:

$$n_d = \frac{2.5}{22} \lambda \quad (19)$$

where  $F$  is Faraday's constant,  $D_w^m$  denotes the diffusivity of the dissolved water in the membrane phase,  $\rho_{Naf}$  and  $EW$  represent the mass density and equivalent weight of the dry Nafion respectively, and  $S_\lambda$  is the source term due to the phase change. The diffusivity of the dissolved water in the electrolyte phase relates to the water content by the following expression [45]:

$$D_w^m = \begin{cases} 3.1 \times 10^{-7} \lambda \left( e^{0.28\lambda - 1} \right) e^{\left( -\frac{2346}{T} \right)} & 0 < \lambda < 3 \\ 4.17 \times 10^{-8} \lambda \left( 161 e^{\lambda + 1} \right) e^{\left( -\frac{2346}{T} \right)} & 3 < \lambda < 17 \end{cases} \quad (20)$$

Likewise, the water content is linked to the molar concentration of dissolved water  $C_{H_2O}^{Naf}$ :

$$\lambda = \frac{EW}{\rho_{Naf}} C_{H_2O}^{Naf} \quad (21)$$

The membrane water content at equilibrium depends on the local water activity and is determined by the following empirical expression [39]:

$$\lambda_{equil} = \begin{cases} 0.043 + 17.18a - 39.85a^2 + 36a^3 & 0 < a < 1 \\ 14 + 1.4(a - 1) & 1 \leq a \leq 3 \end{cases} \quad (22)$$

where  $a$  is the water activity given as follows:

$$a = \frac{y_w P}{P^{sat}} + 2s \quad (23)$$

where  $y_w$  is the water mole fraction,  $P$  denotes the total pressure and  $s$  represents the liquid water saturation.  $P^{sat}$  (in atm) is the saturation pressure, which is related to the temperature [39]:

$$\log_{10} \frac{P^{sat}}{101325} = -2.1749 + 0.02953(T - 273.15) - 9.1837 \times 10^{-5}(T - 273.15)^2 + 1.4454 \times 10^{-7}(T - 273.15)^3 \quad (24)$$

### 2.2.5. Transport of liquid water

PEM fuel cells usually operate at low temperatures (<100°C) and as such liquid water normally exists within porous layers and gas flow channels. Overlooking the occurrence of liquid water in PEMFC model may result in the overprediction of the fuel cell performance. The governing equations for the transport of liquid water in GDL/CLs could be described as [4]:

$$\nabla \cdot \left( \rho_l \frac{k_{rl}}{k_{rg}} \frac{\mu_g}{\mu_l} \vec{u}_g \right) = \nabla \cdot \left( -\rho_l \frac{k_0 k_{rl}}{\mu_l} \nabla p_c \right) + S_l \quad (25)$$

where  $k_{rg}$  and  $k_{rl}$  are the values of the relative permeability of the gas and liquid phases,  $k_0$  is the absolute permeability,  $S_l$  is the source/sink term due to water condensation or vaporization and  $p_c$  is the capillary pressure which is expressed by the following equation:

$$p_c = \sigma \cos \theta_c \left( \frac{\varepsilon}{k_0} \right)^{0.5} J(s) \quad (26)$$

where  $\sigma$  represents the surface tension of the liquid water and  $\theta_c$  denotes the contact angle between the liquid water droplets and the surface of the porous media.  $J(s)$  is the Leverett function, which is employed to account for the effect of liquid water on the capillary pressure [46]:

$$J(S) = \begin{cases} 1.417(1-s) - 2.212(1-s)^2 + 1.263(1-s)^3 & \theta_c < 90^\circ \\ 1.417s - 2.212s^2 + 1.263s^3 & \theta_c > 90^\circ \end{cases} \quad (27)$$

### 2.2.6. Conservation of energy equation

The conservation equation of energy is described as [5]:

$$\nabla \cdot (\rho_g C_p \vec{u} T) = \nabla \cdot (k_T^{eff} \nabla T) + S_T \quad (28)$$

where  $C_p$  represents the specific heat capacity of the gas mixture and is calculated by mixing-law:

$$C_p = \sum \omega_i C_{p,i} \quad (29)$$

$k_T^{eff}$  denotes the effective thermal conductivity, which for the porous media, is calculated as [47]:

$$k_T^{eff} = -2k_s + \left[ \frac{\varepsilon}{2k_s + k_f} + \frac{1-\varepsilon}{3k_s} \right]^{-1} \quad (30)$$

where  $k_s$  and  $k_f$  designate the thermal conductivities of the solid and fluid phases in the GDLs and CLs respectively. Note that, to be in line with the experimental findings,  $k_s$  was set to be anisotropic for the GDLs; see Table 2.

In Eq. (28),  $S_T$  denotes the heat source/sink term, which is caused by the following phenomena: (i) entropic heat, (ii) irreversible heat due to activation and ohmic losses and (iii) latent heat due to water condensation/evaporation [5,46]:

$$S_T = S_{T,ent} + S_{T,act} + S_{T,ohm} + S_{T,con/eva} \quad (31)$$

Unlike the GDLs and the CLs, the heat source term is zero for the gas flow channels. All the sources of generation/consumption of heat are present in the catalyst layers and can be expressed as follows [5,46]:

$$j \left( \eta + \frac{T \Delta S}{nF} \right) + \frac{i_s^2}{\sigma_s} + \frac{i_m^2}{\sigma_m} + S_1 h_{fg} \quad (32)$$

where  $h_{fg}$  is the latent heat of water condensation/evaporation, and  $S_1$  is the source term of liquid water [48]:

$$S_1 = A_{pore} \frac{Sh_c D_w}{\bar{d}} (1-s)(\rho_w - \rho_{sat})q + A_{pore} \frac{Sh_e D_w}{\bar{d}} s(\rho_w - \rho_{sat})(1-q) \quad (33)$$

where  $A_{pore}$  is defined as the pore surface area per volume,  $\bar{d}$  is characteristic length of water diffusion in the vicinity of phase change interface,  $\rho_{sat}$  is the density of saturated water and  $q$  is switching function (which is 1 for the water partial pressure larger than the saturation pressure and 0 otherwise) is given as follows [49]:

$$q = \frac{1 + |(\rho_v - \rho_{\text{sat}})| - (\rho_v - \rho_{\text{sat}})}{2} \quad (34)$$

All the source/sink terms appeared in the transport governing Eqs. (1), (2), (3), (9), (10), (18), (25) and (28) are listed in Table 3.

**Table 3** Source/sink terms of transport governing equations in the developed PEMFC model.

Source term	Equation	Equation No.
Momentum source term of gas phase	$S_m = -\frac{\mu_g}{k_{rg} k_0} \vec{V}_g$ (in all porous layers)	(35)
Hydrogen mass source term	$S_{H_2} = -\frac{j_a}{4F} M_{H_2}$	(36)
Oxygen mass source term	$S_{O_2} = -\frac{j_c}{4F} M_{O_2}$ (in CCL)	(37)
Water vapour mass source term	$S_{H_2O} = \begin{cases} -S_{\text{phase}} - S_\lambda M_{H_2O} & \text{(in ACL)} \\ -S_{\text{phase}} & \text{(elsewhere)} \end{cases}$	(38)
Ionic transport source term	$S_{\phi_s} = \begin{cases} -j_c & \text{(in CCL)} \\ j_a & \text{(in ACL)} \end{cases}$	(39)
Electrical transport source term	$S_{\phi_m} = \begin{cases} j_c & \text{(in CCL)} \\ -j_a & \text{(in ACL)} \end{cases}$	(40)
		(41)
Heat source term	$S_T = \begin{cases} j \left( \eta + \frac{T \Delta S}{nF} \right) + \frac{i_s^2}{\sigma_s} + \frac{i_m^2}{\sigma_m} + S_1 h_{fg} & \text{(in CLs)} \\ \frac{i_s^2}{\sigma_s} + S_1 h_{fg} & \text{(in GDLs)} \\ \frac{i_m^2}{\sigma_m} & \text{(in membrane)} \end{cases}$	(42)
Dissolved water mass source term	$S_\lambda = \begin{cases} r_c \frac{\rho_{\text{Neff}}}{EW} (\lambda_{\text{equal}} - \lambda) + \frac{j_c}{2F} & \text{(in CCL)} \\ r_a \frac{\rho_{\text{Neff}}}{EW} (\lambda_{\text{equal}} - \lambda) & \text{(in ACL)} \end{cases}$	(43)

---


$$\begin{aligned}
\text{Liquid water} \\
\text{mass source term}
\end{aligned}
S_1 = \begin{cases}
A_{\text{pore}} \frac{Sh_c D_w}{d} (1-s) (\rho_w - \rho_{\text{sat}}) q \\
+ A_{\text{pore}} \frac{Sh_e D_w}{d} s (\rho_w - \rho_{\text{sat}}) (1-q) + \left( \frac{j_c}{2F} - S_\lambda \right) M_{H_2O} \quad (\text{in CCLs}) \\
A_{\text{pore}} \frac{Sh_c D_w}{d} (1-s) (\rho_w - \rho_{\text{sat}}) q \\
+ A_{\text{pore}} \frac{Sh_e D_w}{d} s (\rho_w - \rho_{\text{sat}}) (1-q) \quad (\text{in GDLs})
\end{cases} \quad (44)$$


---

### 2.3. Boundary conditions

No-slip and zero flux boundary conditions were applied for the velocity and species transport equations on all the external surfaces.

The cathode and anode inlet velocities are described as [5]:

At the anode:

$$u_{a, \text{in}} = \theta_a \frac{I_{\text{ave}}}{2F} A \frac{RT_{a, \text{in}}}{P_{a, \text{in}}} \frac{1}{x_{h, \text{in}}} \frac{1}{A_{\text{ch}}} \quad (45)$$

At the cathode:

$$u_{c, \text{in}} = \theta_c \frac{I_{\text{ave}}}{4F} A \frac{RT_{c, \text{in}}}{P_{c, \text{in}}} \frac{1}{x_{o, \text{in}}} \frac{1}{A_{\text{ch}}} \quad (46)$$

where  $\theta_a$  and  $\theta_c$  represent the flow stoichiometric ratio of hydrogen and oxygen, respectively,  $A$  is the active surface area and  $A_{\text{ch}}$  denotes the cross-sectional area of the flow channels. Potentiometric boundary conditions were used for the present PEMFC model: electrical potential values were imposed as zero and  $V_{\text{cell}}$  at the anode and the cathode terminals. The pressure outlet condition was used for the outlets of the flow channels. The symmetry boundary conditions were applied to the left and right planes of the computational domain.

### 2.4. Model implementation

The set of the steady-state governing equations described above were discretized by adopting the finite volume method (FVM) on a structured computational grid using hexahedral cells generated by Gambit 2.4. The fuel cell model was solved using a commercial CFD package, FLUENT 14.0 (Ansys Inc. USA) through user-defined functions (UDFs) and user-defined scalars (UDS). Four general scalar equations were

defined using a set of user defined scalar (UDS) to represent four underlying conservation equations, namely: transport of electrons, protons, dissolved water and liquid water. The source/sink terms in the underlying equations, the mixture properties, boundary conditions for the channels inlet and outlet, in addition to the anisotropic values of the permeability, electrical and thermal conductivities were defined using UDFs, which was written in C programming language and was compiled in Fluent. The SIMPLE (semi-implicit method for pressure-linked equations) algorithm was selected for coupling velocity-pressure equations. A second-order upwind discretization scheme was used for all the underlying equations. The iterative procedure was kept running until all the scaled residuals were below  $1 \times 10^{-6}$ . In addition, the convergence check strategy for modeled PEMFCs based on the species mass flux and current density in addition to the residual monitoring proposed by Arvay et al. [50] was used to ensure a converged solution. The PC used to perform the computations was a 2.4 GHz Intel Core i5 CPU with 4 GB RAM and Windows 7 operating system.

## **2.5. Grid independency test**

A stringent grid study method similar to the one in our previous work [51] was adopted for the present study. For the geometry cases with the blockage and metal foam flow-field distributors, a fine mesh (both in y- and x-directions) was applied near to the blocks and the metal foam channels. The solutions were found to be independent of the grid which consists of 50 and 80 cells in x- and z-directions respectively and of 8-10 cells for each of the components in y-direction. The final meshes for the computations cases were as follows: ~ 412,000 cells for the parallel, ~412,000 for the interdigitated, ~412,000 for the serpentine, ~460,000 for the staggered and ~530,000 for the metal foam flow field case. The meshed geometry of the serpentine flow field case is shown, as an example, in Fig. 2.

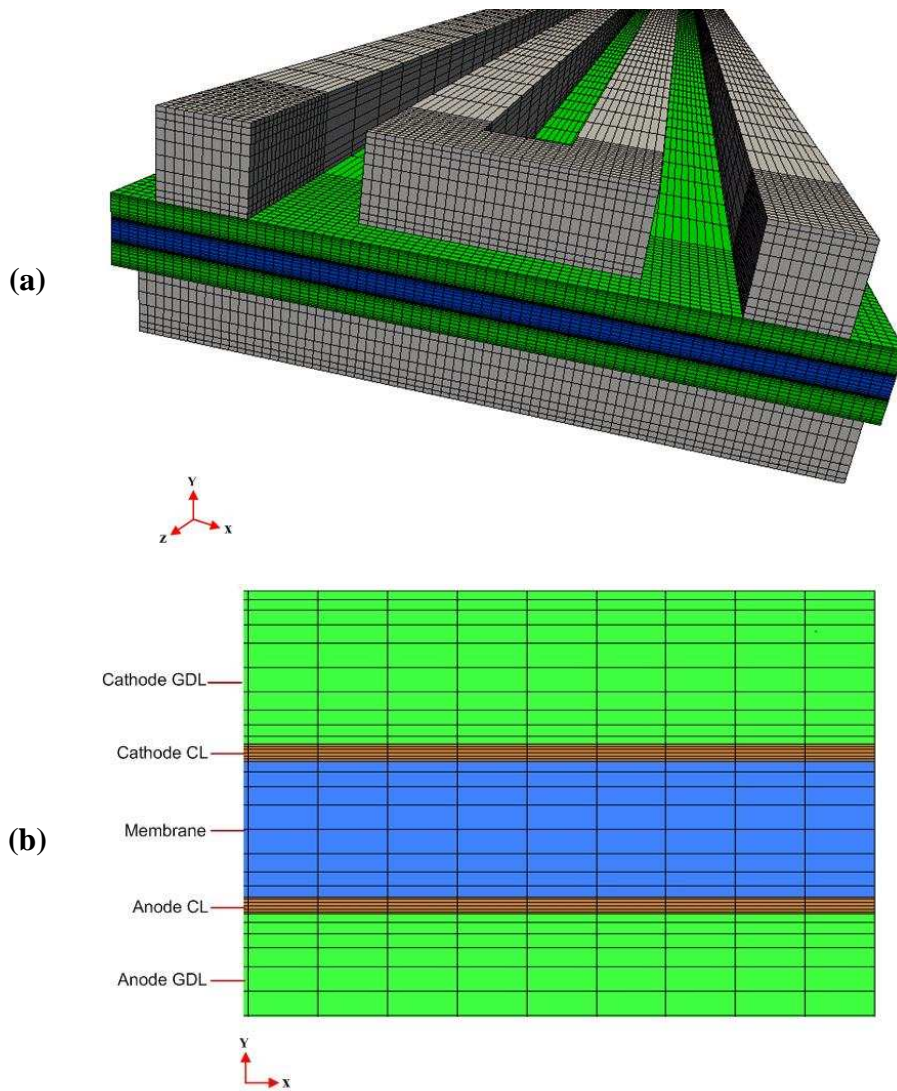


**Fig. 2.** The meshed geometry of the serpentine flow field case: (a) 3D view and (b) the distribution of the cells across the various components of the membrane electrode assembly.

### 3. Results and Discussion

#### 3.1. Model validation

To validate the PEM fuel cell model developed here, the simulated results of the model are compared to those values obtained experimentally by Wang et al. [52], as illustrated in Fig. 3. Note that the conventional parallel flow field configuration was used for the model and all the dimensions and operating conditions were chosen to be the same as those of the experiments [52]. As depicted in Fig. 3, the values predicted by the PEMFC

model are in good agreement with those values collected from the literature with some small disparities at low current densities (less than  $0.4 \text{ A/cm}^2$ ), which it may be ascribed to the use of the kinetic model (i.e., simple Butler-Volmer) used in this work, which does not take into account the microporous structure of the catalyst layer. This, however, does not significantly affect the output of the developed PEM model since the operating voltage used for the simulations is far from those zones.

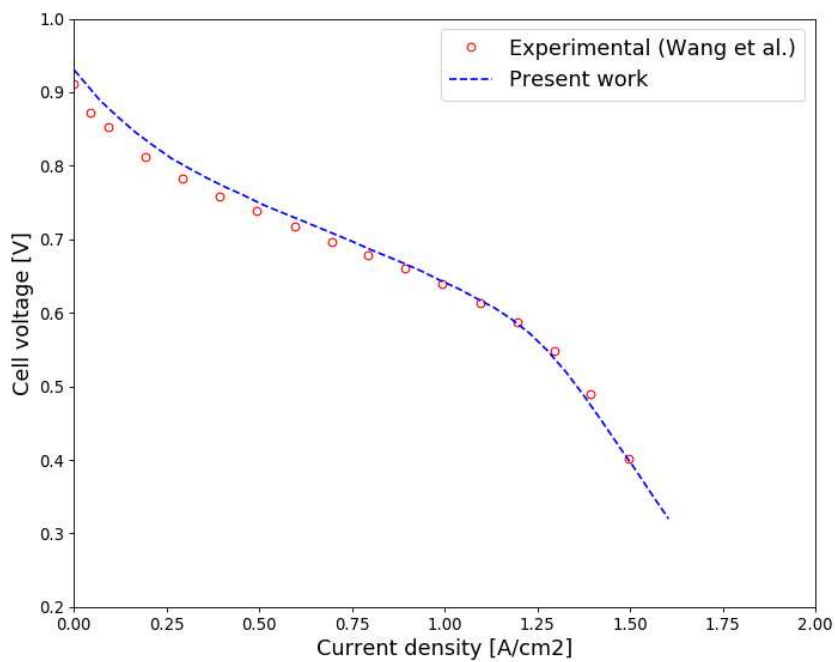


**Fig. 3.** The modeling values as compared to the experimental data presented by Wang et al. [52].

### 3.2. Comparing different flow field designs

An efficient flow field design—especially at the cathode—is a practical solution to efficiently manage water and heat within the fuel cell. An optimally-designed flow field impedes reactants maldistribution on the CLs, leading to lower pressure drop along the flow channels, which enhances the proton conductivity of the membrane and more efficient water balance. In the following, we compare the simulation results of different

types of cathode flow fields used in the modeled PEM fuel cell. To this end, contour diagrams showing the distribution of temperature, current density, oxygen concentration, and liquid water, as well as concentration polarization curves, were all generated for all the cases. Aside from the average and maximum values of the characteristic variables in a fuel cell as mentioned above, the uniform distribution of these variables is also important. As such, an area-weighted uniformity index was used to compare the investigated flow fields in terms of uniformity which its integral form is described as:

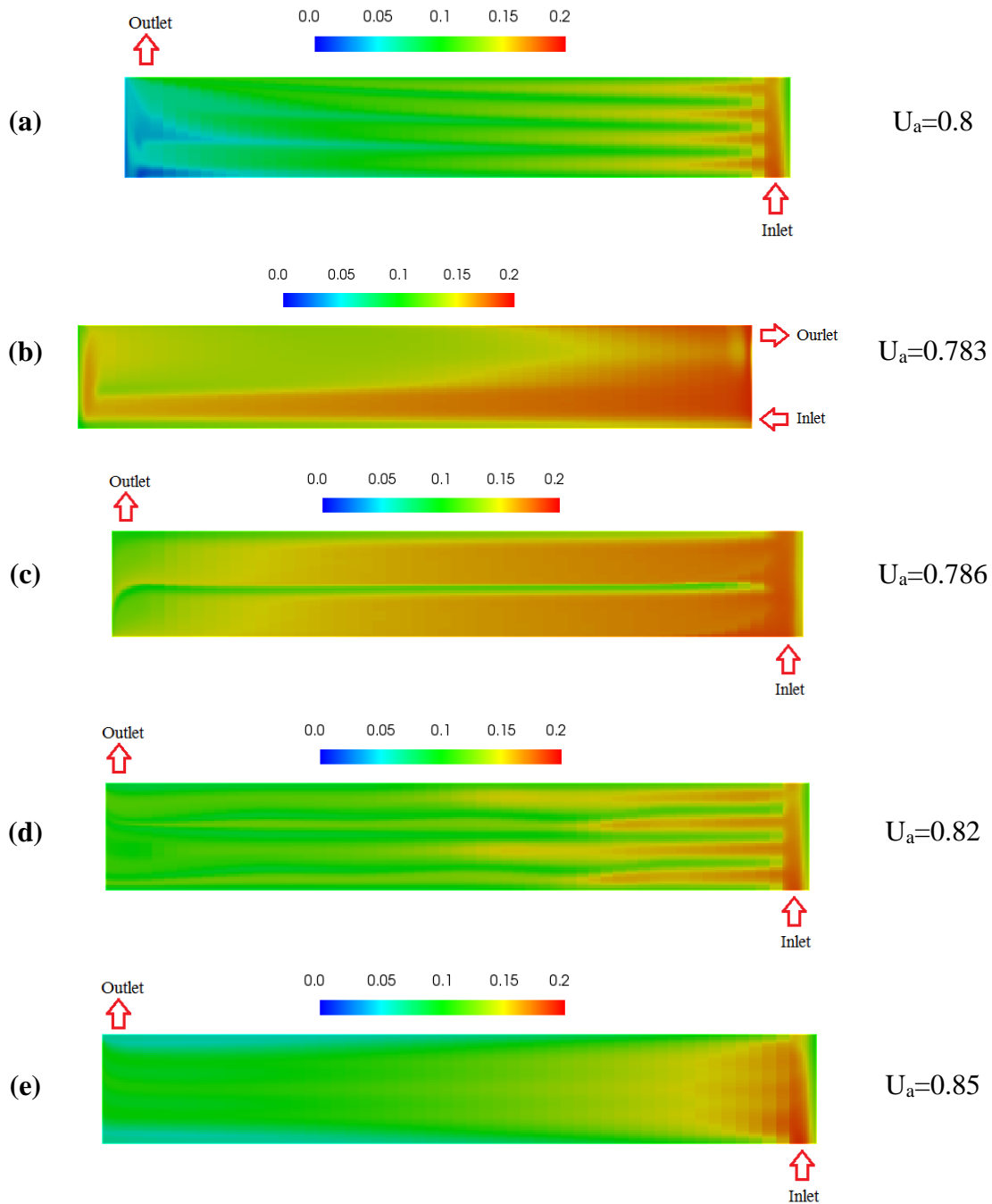
$$U_a = 1 - \frac{\int_s |J - J_{avg}| ds}{2 \int_s J_{avg} ds} \quad (47)$$

Where  $ds$  is the surface of interest (here, the interface between CL-GDL),  $J$  is the local value of that variable and  $J_{avg}$  is also defined as:

$$J_{avg} = \frac{\int_s J ds}{\int_s ds} \quad (48)$$

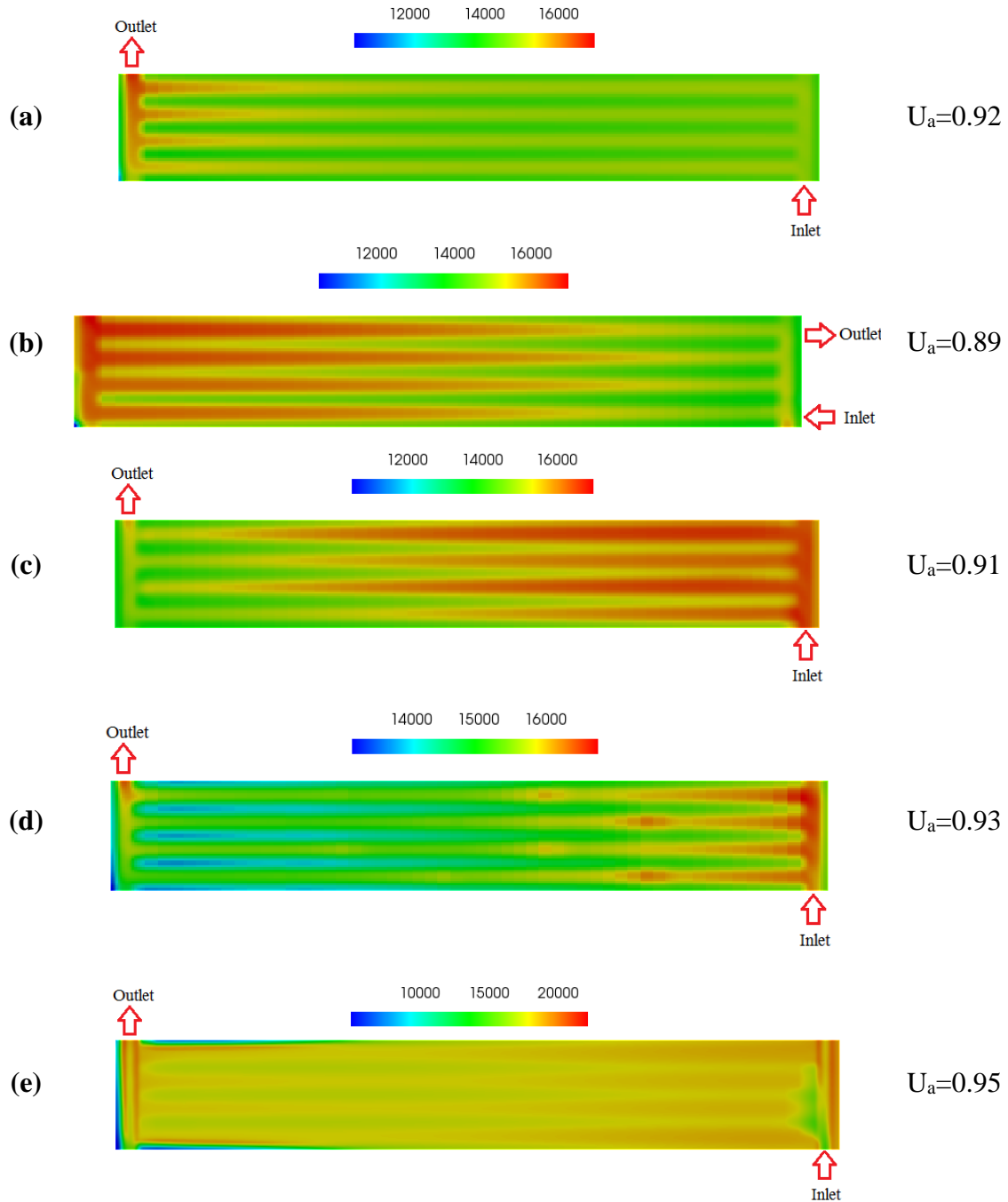
This index is used to represent the variation of a field variable on a specific surface. Thus, the closer the index uniformity to 1 indicates the more uniform distribution of that variable. As fuel cell operates, oxygen fed into the flow channels passes through the GDL and reaches to the CL layer where it consumes due to the electrochemical reaction. The contribution of an efficiently-designed flow field distributor is more highlighted as operating voltages decreases. The distribution of oxygen mass fraction at the interface between the cathode GDL and CL layer at  $V_{cell} = 0.4V$  is depicted in Fig. 4. As illustrated, the oxygen concentration reduces along the channel length for all the simulated cases, but the intensity is not the same. Comparatively speaking, one sees that the basic parallel flow field suffers from oxygen depletion at the downside of the cell; apparently this oxygen maldistribution is offset with other types of flow fields to a different extent. Evenly distribution of oxygen is equally important as its average value to avoid locally undesirable phenomena. The values of uniformity index of oxygen

concentration at the CL-GDL interface calculated and are given in Fig. 4. To better see the performance of the selected flow fields, the distribution of current density should also be considered along with the oxygen contours of the mass fraction.



**Fig. 4.** Contours of oxygen mass fraction at the GDL/ CL interface along with its uniformity index for the cases incorporating cathode flow field of (a) single parallel, (b) single-pass serpentine, (c) interdigitated, (d) parallel with blocks and (e) metal foam.

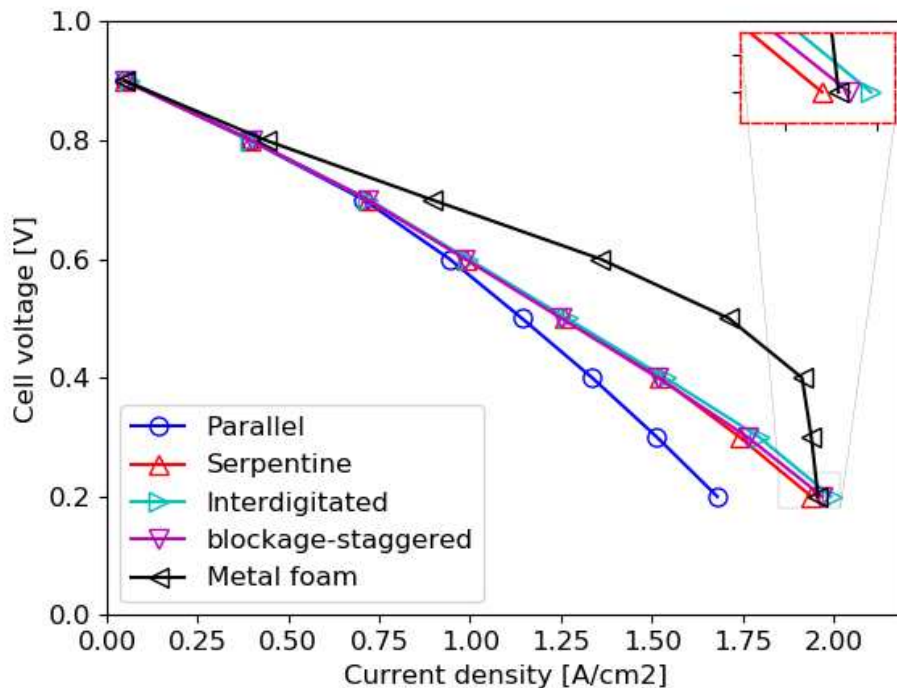
The uniform distribution of current density is an important issue in a fuel cell which should be taken into consideration when designing the flow fields. A uniformly distributed current density prevents the formation of hot spot zones inside the MEA and hence increases the fuel cell durability. The distribution of current density magnitudes at the GDL/CL interface for the flow fields considered here are depicted in Fig. 5. One can see that the current density distribution is more or less similar to the oxygen distribution in all the cases. Corresponding to Fig. 5, it can be seen that the most uniform current density distributions are those with parallel and metal foam flow distributors. On the other hand, the flow fields with the interdigitated and serpentine layouts show the least uniform current density at the GDL/CL interface. This may be explained by different dominant transport mechanisms in the flow channels of each investigated cases. The current density distribution in the modeled flow fields is influenced by the oxygen distribution and the extent of cross-flow in the areas between the flow channels. Diffusion is the main mode of transport of oxygen across the GDL with the parallel layout. On the other hand, due to presence of cross-flow beneath the ribs of the flow-field plates, oxygen is more transported through the GDL by convection with the interdigitated flow layouts or by a combination of diffusion and convection with serpentine (i.e. diffusion remains the main mode of transport with the serpentine flow field layout, given that permeability is less than  $10^{-13} \text{ m}^2$ ), parallel with staggered blocks and metal foam layouts. As seen in Fig. 4, the oxygen distribution shows better uniformity with the metal foam layout. Also, the oxygen distribution in parallel layout with staggered blocks is rather uniform as the blocks enhance the cross-flow of oxygen within the GDL compared to the straight parallel design.



**Fig. 5.** Contours of current density distribution at the GDL/ CL interface for the cases incorporating cathode flow field of (a) single parallel, (b) single-pass serpentine, (c) interdigitated, (d) parallel with blocks and (e) metal foam. The values are in ( $A/m^2$ ).

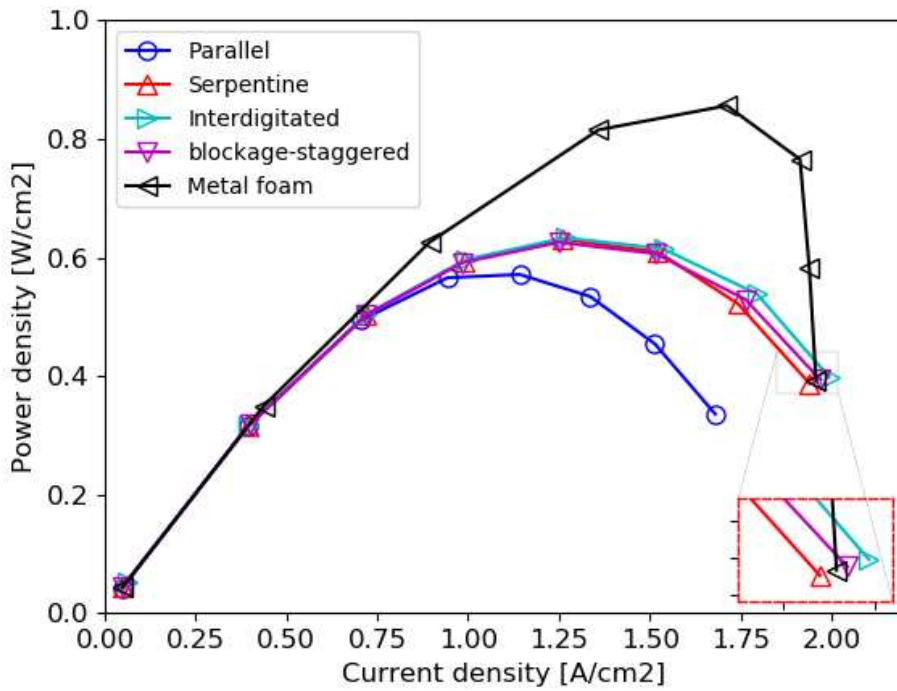
As illustrated in Fig. 5, the magnitude of the current density is larger under lands and the borders between the lands and the flow channels and it is smaller at the centers of the channels. Such profile is linked to the profile of oxygen shown in Fig. 4 where the areas with relatively low concentrations of oxygen reflect a high rate of oxygen consumption

and subsequently high current densities. At 0.4 V, the averaged values of the oxygen mass fractions at the channel outlet are 0.108, 0.068, 0.054, 0.085, and 0.042 for the modeled fuel cell with parallel, serpentine, interdigitated, parallel with staggered blocks and metal foam layout. The reported values clearly show the efficiency of different flow fields to mitigate oxygen exhaust to the channel outlet by pushing oxygen to the CL layers. The polarization curves in Fig. 6 may be roughly divided into three main regions: activation losses dominant region ( $>0.8$  V); Ohmic losses dominant region ( $0.6 < V < 0.8$ ); and mass transport losses dominant region ( $<0.5$  V). The difference in cell performance between the cases is much more profound in the last region. As demonstrated in Fig. 6, at mass transport region, the case with the metal foam flow field portrays the best performance and the case with the parallel flow field shows the worst performance. Fig. 6 also shows that the cases with the serpentine, interdigitated and parallel with staggered-blocks flow fields have similar and comparable trends for operating voltages less than 0.6 V.



**Fig. 6.** Effect of flow field design on the polarization curve of the modeled fuel cell.

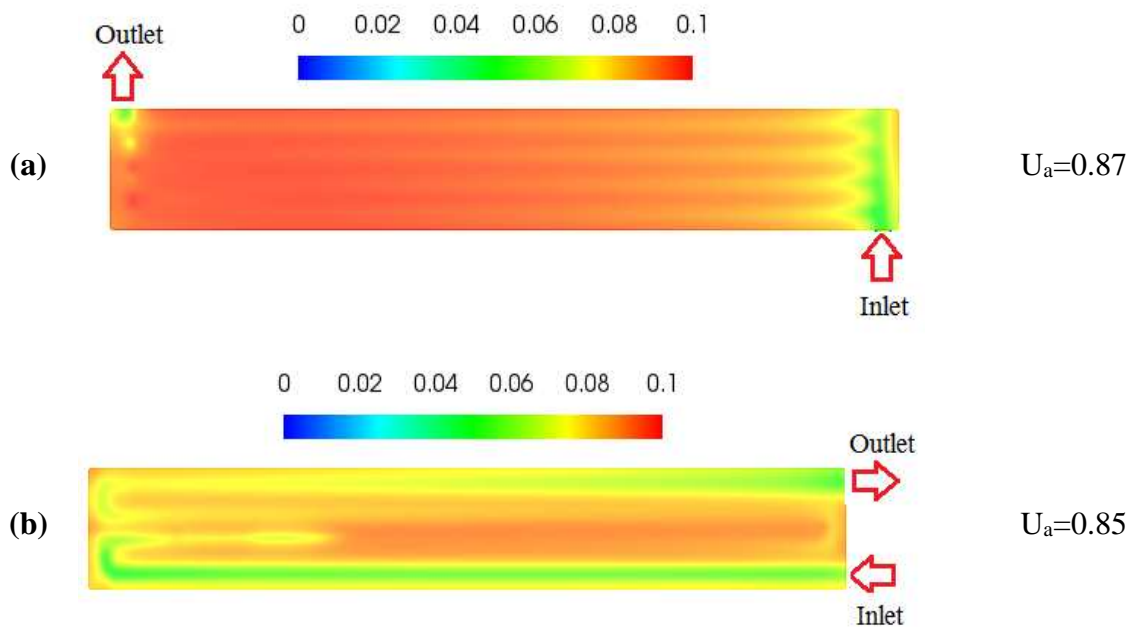
Fig. 7 shows the power density curves for the investigated cases. As shown in this figure, the metal foam and the basic parallel flow field configurations demonstrate the maximum and the minimum peak power densities respectively. Quantitatively speaking, the maximum power density obtained by the metal foam flow field is nearly 50% more than the value for the basic parallel distributor. As will be shown later when discussing the water saturation profiles, the superiority of the metal foam design over the other investigated designs is due to the lowest liquid water saturation demonstrated by the metal foam design, thus decreasing the mass transport resistance and allowing more reactant gas of oxygen to reach the catalyst layer. On the other hand, relative to the basic parallel flow field, the performance gain when using the serpentine, interdigitated and staggered blockage flow fields is about 10%. Before moving to the discussion of the key variables, it is noteworthy that, if not properly surface-treated, metal foam may suffer from corrosion which potentially affects the long-term performance of the fuel cell. The capture of the physics of the corrosion clearly requires the model to be transient; this is beyond the scope of this study which assumes the fuel cell operation to be steady-state.

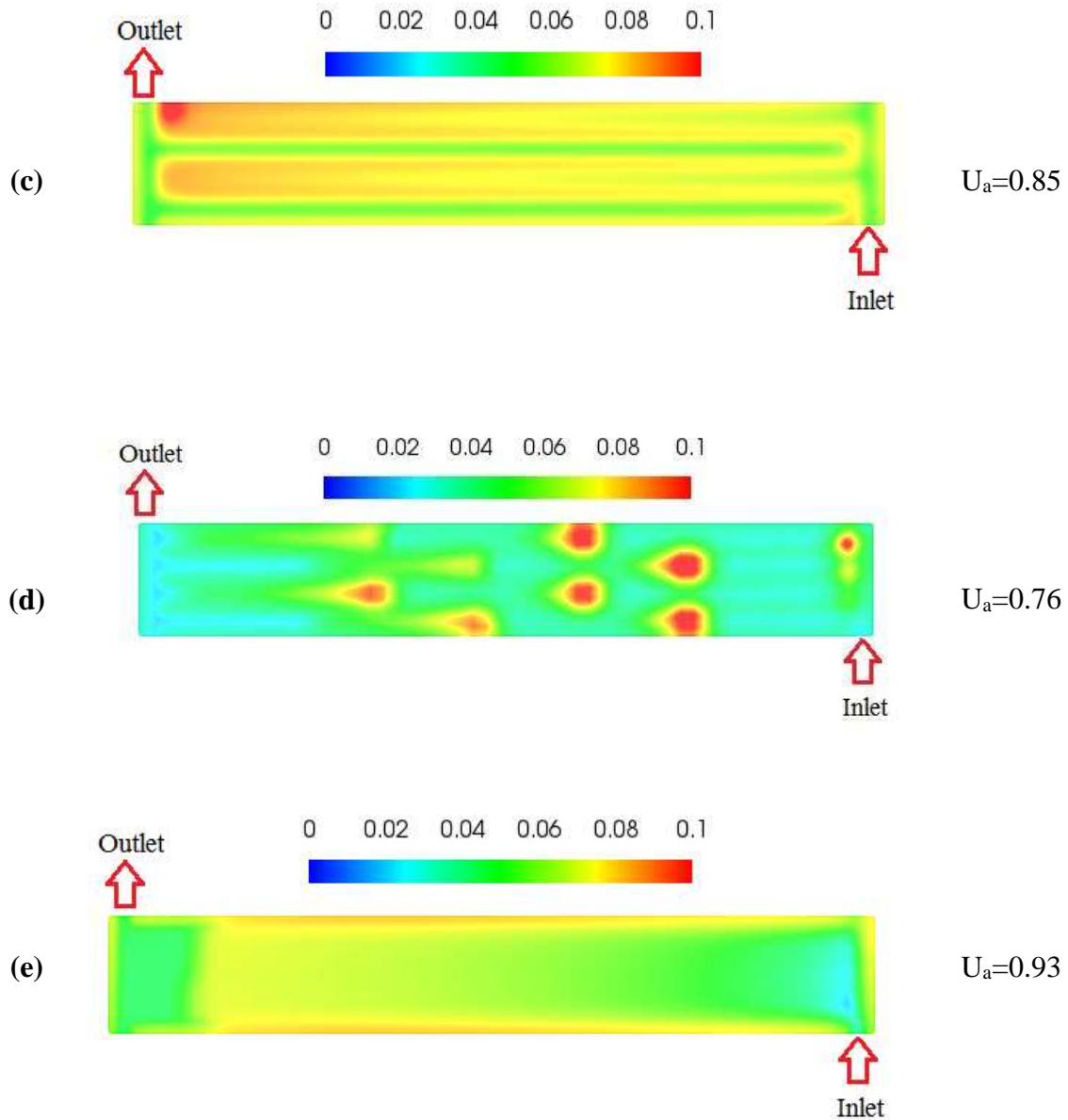


**Fig. 7.** Effect of flow field design on the power density of the modeled fuel cell.

The distribution of liquid water at the interface between the cathode GDL and CL for the investigated cases is presented in Fig. 8. As depicted in the latter figure, water saturation is in general, higher under the areas lying beneath the ribs and near to the channel walls and corners than those under the flow channels. This is most likely due to the relatively weak convective flow under the land areas and the corresponding contours of temperature (Fig. 9). The disparity in liquid water distribution in the investigated layouts is mainly because of the different flow mechanisms dominated in each of these flow configurations induced by the pressure drop as well as temperature distribution. As temperature rises, saturation pressure of water increases, water activity and accordingly liquid water concentration decreases. Notably, the relatively high water saturation that features the parallel flow field signifies its lower efficiency in draining out liquid water and justifies the lower fuel cell performance as cell's operating voltage decreases (see Fig. 6). This is associated with relatively low-pressure drop and predominately diffusion transport

mechanism with the parallel flow field. Comparatively, the relatively large pressure drop with the serpentine layout is attributed to the long pathway with turning points that the fluid requires to pass through. This improves the convective cross flow and therefore pushes liquid water out from the gas diffusion layers and flow channels more effectively. The design of the interdigitated flow field causes strong convective cross-flow between the adjacent channels which significantly improves the removal of liquid water present in the GDLs and the flow channels. As for the parallel flow field with blocks, water saturation tends to be high at the areas beneath the blocks owing to the stagnant flow caused by the blocks, resulting in the lowest value of saturation uniformity index; see Fig. 8 (d). It is also worth to note that the metal foam flow field shows the lowest values and the best uniformity of water saturation and this is obviously due to the uniformity of the structural features of the metal foam (i.e., relatively high porosity, thermal conductivity).

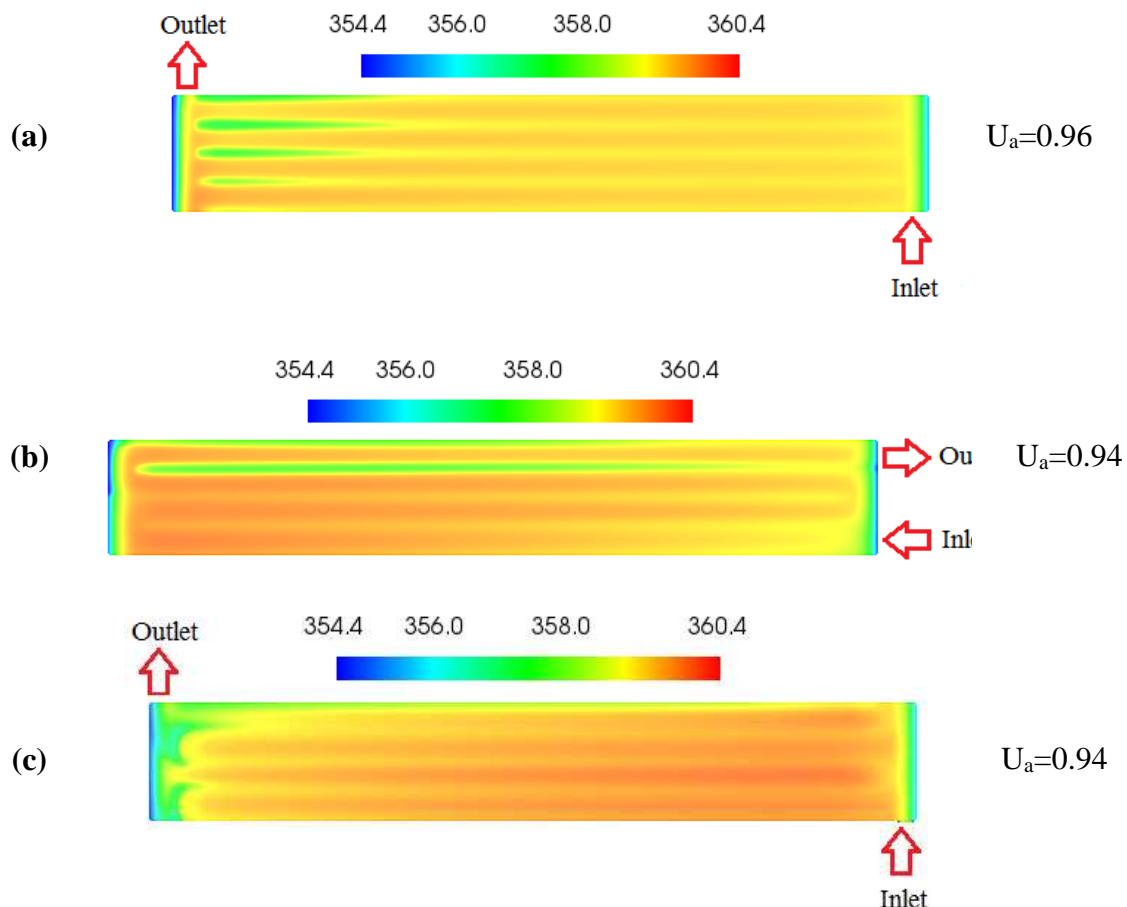




**Fig. 8.** Contours of water saturation at the GDL/CL interface for the cases incorporating cathode flow field of (a) single parallel, (b) single-pass serpentine, (c) interdigitated, (d) parallel with blocks and (e) metal foam.

Temperature is highly linked to the formation of liquid water in PEM fuel cells. Relatively low temperatures may result in high water saturation and in critical conditions may lead to water flooding particularly at the cathode. On the other hand, relatively high temperatures may alleviate the possibility of water flooding issue but may also cause membrane dehydration. Also, uniformity of temperature is equally important to prevent some undesirable phenomena such as hot spots and thermal degradation. Thus, finding

optimum values for the temperature of the fuel cell is important especially at medium to low operating voltages where the generation of water and heat is more salient. Contours of temperature at the interface between the cathode CL and the membrane for the investigated cases are depicted in Fig. 9. A look at Fig. 5 and Fig. 9, one reveals that the temperature distribution profile in the studied flow fields is more or less similar to the profile of current density in Fig. 5. As such, those areas with the locally highest current density magnitudes in Fig. 5 correspond to the temperature with the highest values and vice versa. As illustrated in the figure, the flow fields with serpentine, interdigitated and parallel with blocks, generally demonstrate the highest values of temperature whereas the flow with parallel and the metal foam show the lowest values. Interestingly, the metal foam flow field shows the most uniform temperature profiles and this is obviously due to the relatively high degree of structure uniformity in this type of flow field.



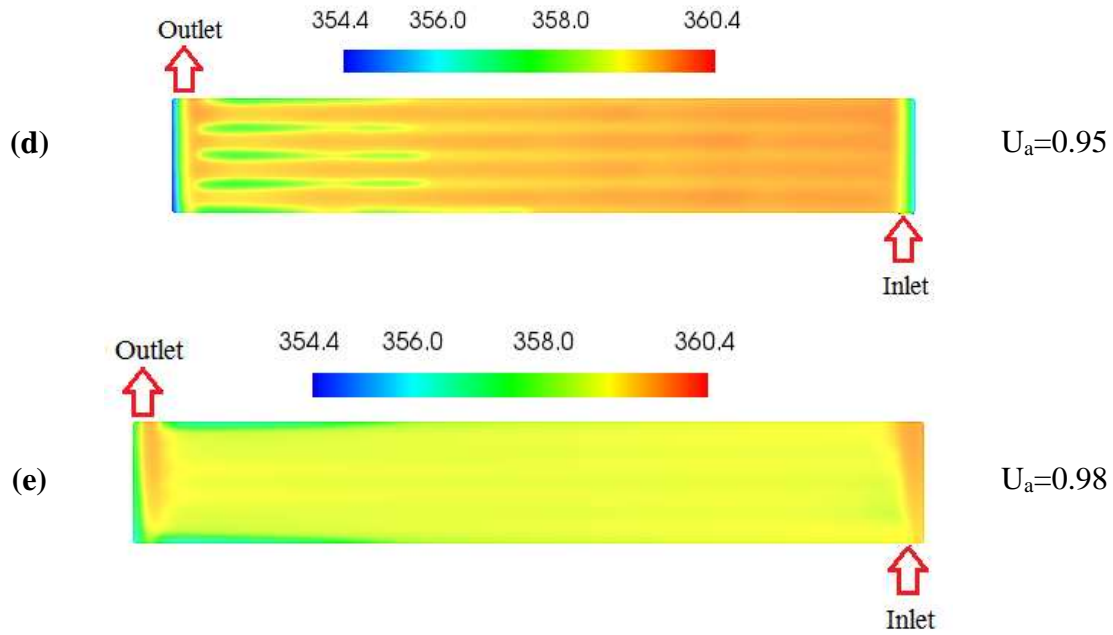


**Fig. 9.** Contours of temperature at the GDL/ CL interface for the cases incorporating cathode flow field of (a) single parallel, (b) single-pass serpentine, (c) interdigitated, (d) parallel with blocks and (e) metal foam.

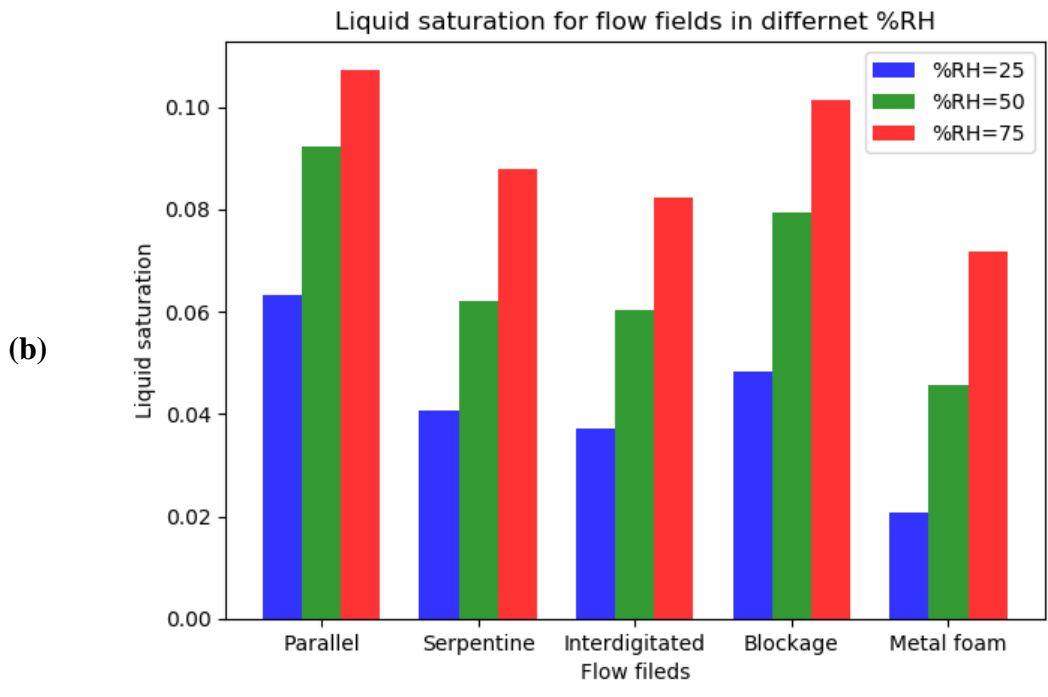
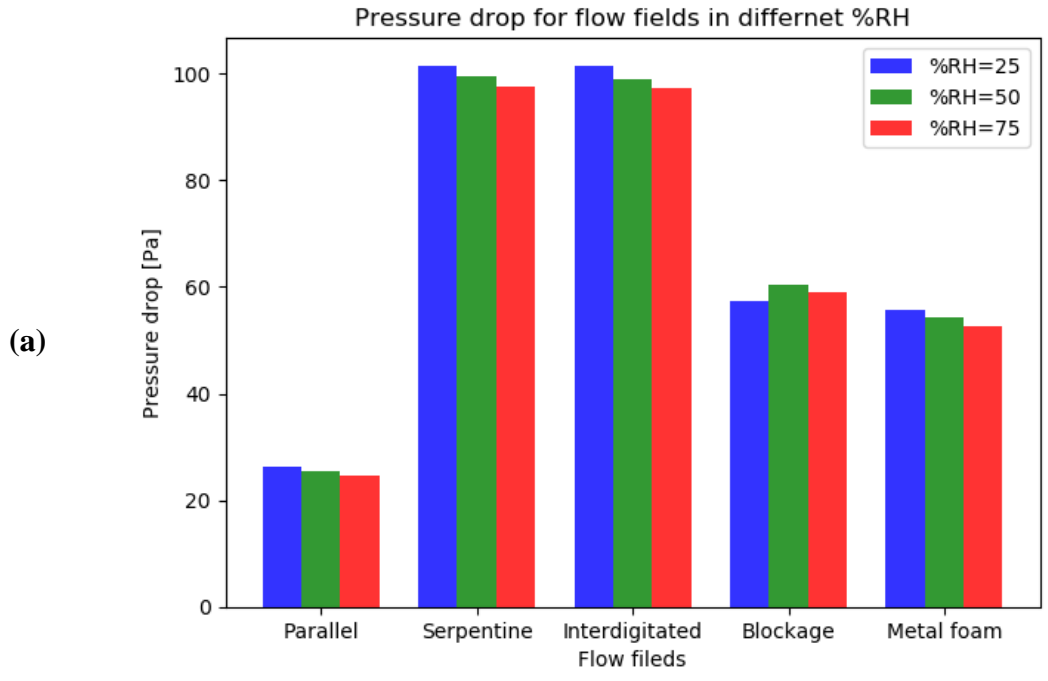
### 3.3. Parametric analysis

The fuel cell performance with different flow fields varies under different operating conditions. To gain a better insight of the performance of the cathode flow field distributors used in the present work, we conducted a series of simulations for different operating conditions of the cathode inlet flow, namely relative humidity (RH), flow stoichiometry ratio (SR) and inlet flow temperature; the results of which are compared and discussed below.

#### 3.3.1. Effect of cathode relative humidity (RH)

In this section, we investigate the impact of cathode relative humidity on pressure drop, water saturation and power density obtained for each of the modeled flow fields at a cell operating voltage of 0.4 V. In PEMFC systems, in addition to obtaining high performance and uniform distribution of current density, maintaining an optimum pressure drop across the flow channels is equally important. An optimum pressure drop which reasonably mitigates water flooding and, at the same time, incurs a minimum parasitic loss is of

interest. Fig. 10(a) shows the computed pressure drop obtained for the flow fields for different values of relative humidity. As presented, for all the three cases of RH (i.e. 25, 50 and 75%), the highest values of pressure drop relate to the flow fields with serpentine and interdigitated flow patterns, and the lowest values of pressure drop occur for the basic parallel flow design. The highest pressure drop values are attributed to the relatively long pathway of the serpentine flow-field and to the presence of dead-end channels in the case of the interdigitated flow-field. As expected, the lowest values of the pressure drop are those of the parallel flow field, which is caused by the relatively short pathways between the inlets and the outlets. The values of the pressure drop associated with the partially-blocked parallel and metal foam flow field designs are between the two extreme values demonstrated by the above flow-fields. It should be noted that the sensitivity of the pressure drop to the relative humidity is almost negligible for all the investigated flow-fields. Efficient removal of liquid water from the flow channels is an important characteristic of an appropriately-designed flow field. The effect of cathode relative humidity on water saturation for the five flow fields was evaluated and presented in the form of volume-integrated water saturation in cathode CL; see Fig. 10(b). It can be seen that, for all the cases, liquid water accumulation increases as the inlet relative humidity at cathode increases. Also, it is worth to note that serpentine and interdigitated flow fields show the same trend with liquid water saturation. Moreover, the parallel and the partially-blocked parallel flow fields show the highest liquid water saturation, compared to other designs, which could be attributed to the relatively low-pressure drop for parallel flow field and accumulation of liquid water beneath the blocks of the partially-blocked parallel flow field. Further, the metal foam flow-field demonstrates the least liquid water saturation and this is due to the relatively high convective flow throughout the body of the metal foam.



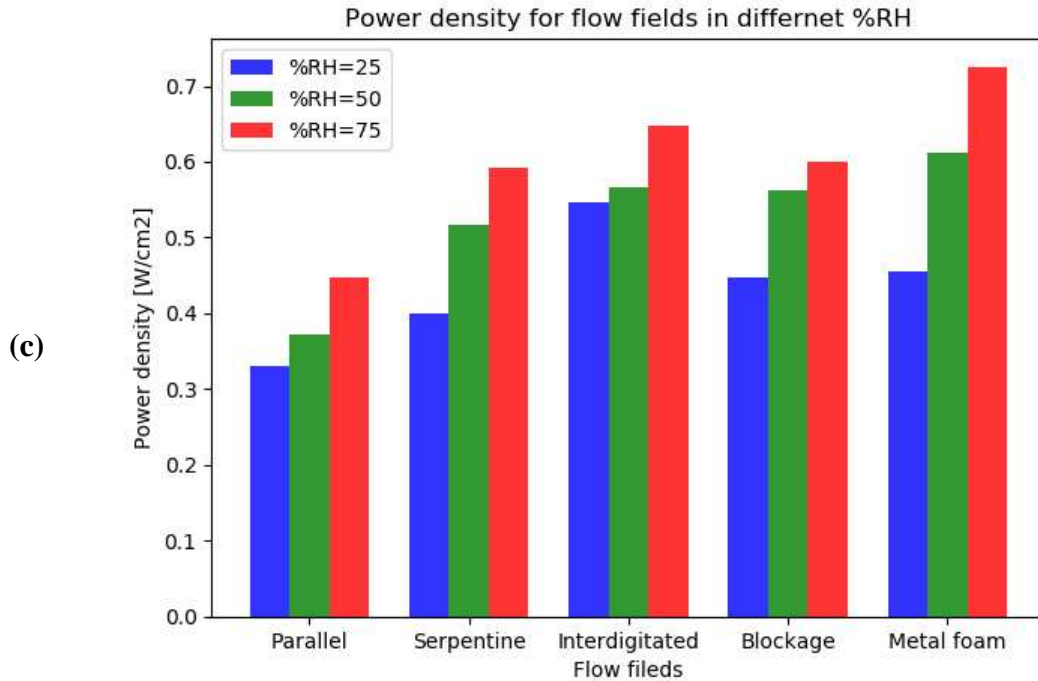


**Fig. 10.** Effects of the relative humidity of cathode inlet gas for different flow fields: (a) total pressure drop (Pa), (b) water saturation and (c) power density (W/cm<sup>2</sup>).

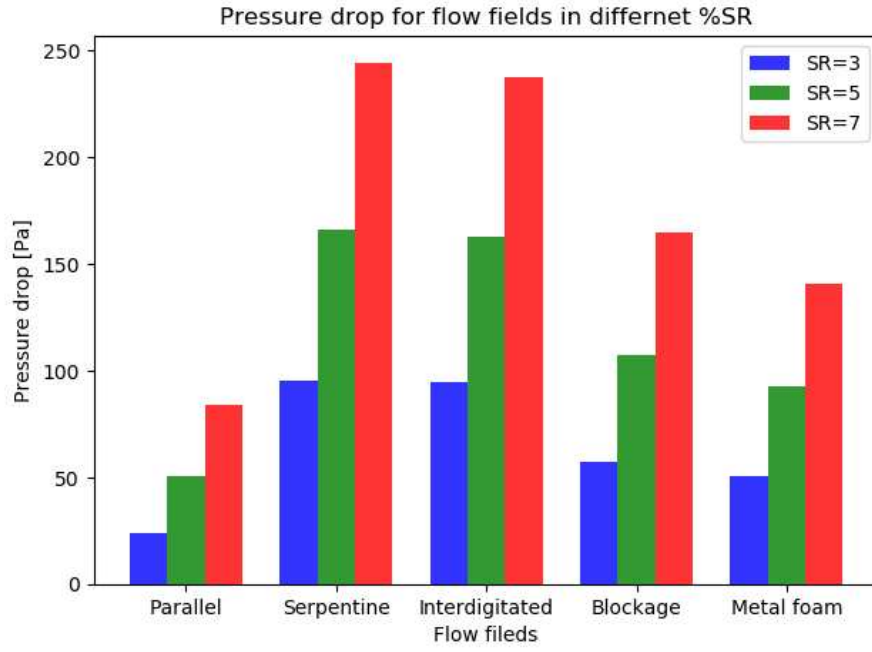
The impact of cathode relative humidity on the output power density for all the studied flow fields is shown in Fig. 10 (c). As shown, the power density generally enhances as the cathode relative humidity increases which is attributed to the enhancement in the humidification of the membrane electrolyte, thus increasing the membrane conductivity and overall cell performance. One could see that the metal foam flow field demonstrates the best power density at intermediate (i.e. 50%) and high (i.e. 75%) relative humidity while the interdigitated flow field show the best power density at a low relative humidity (i.e. 25%). One explanation for this may be the balance between the oxygen transfer to the CLs and the water content for the membrane humidification. In other words, it can be attributed to the more sensitivity of the interdigitated design to the change of RH and thus change in oxygen concentration to the cathode CL compared with others.

### 3.3.2. Effect of cathode flow stoichiometric ratio (SR)

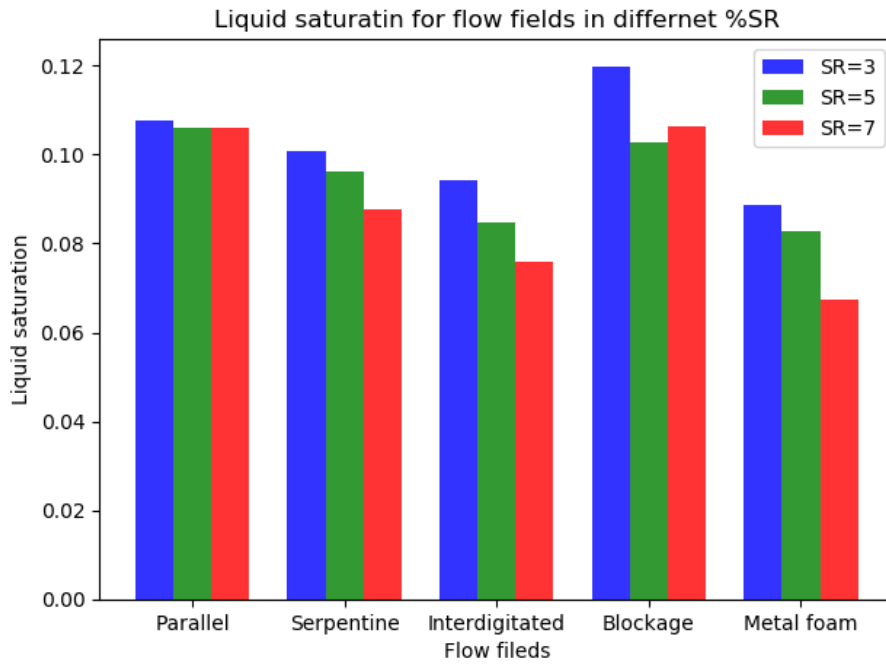
The impact of stoichiometric ratio (SR) of the cathodic flow on the pressure drop, liquid water saturation and power density for different flow field designs are presented in Fig.

11. It can be seen that, for all the investigated flow fields, the pressure drop within the flow channels increases proportionally as the stoichiometric ratio increases. Compared with Fig. 10 (a), it is clear that the pressure drop is much more sensitive to the cathodic stoichiometric ratio than to the relative humidity. The change of volume-integrated liquid water saturation at cathode CL with flow stoichiometric ratio for the investigated flow fields is presented in Fig. 11(b). As demonstrated in the latter figure, the serpentine, interdigitated and metal foam flow fields behave almost the same: the liquid water saturation decreases as stoichiometric ratio increases. This could be attributed to the relatively increased capacity of water removal, induced by relatively high convective flow, in the above flow fields. Also, one could observe that, with parallel flow field, the liquid water saturation is almost insensitive to the cathode flow stoichiometric; this is due to the relatively low contribution of the convective to the total flow. On the other hand, it appears that, for the partially-blocked parallel flow field, there exists an optimum stoichiometric ratio at which the liquid water saturation is a minimum; this seems to be the point at which the supply of both oxygen (necessary for chemical reaction) and water (necessary for the membrane humidification) is adequately ensured. Compared with Fig. 10 (b), it could be clearly seen that the liquid water saturation is more sensitive to the cathodic relative humidity than to the stoichiometric ratio of the cathodic flow.

(a)



(b)



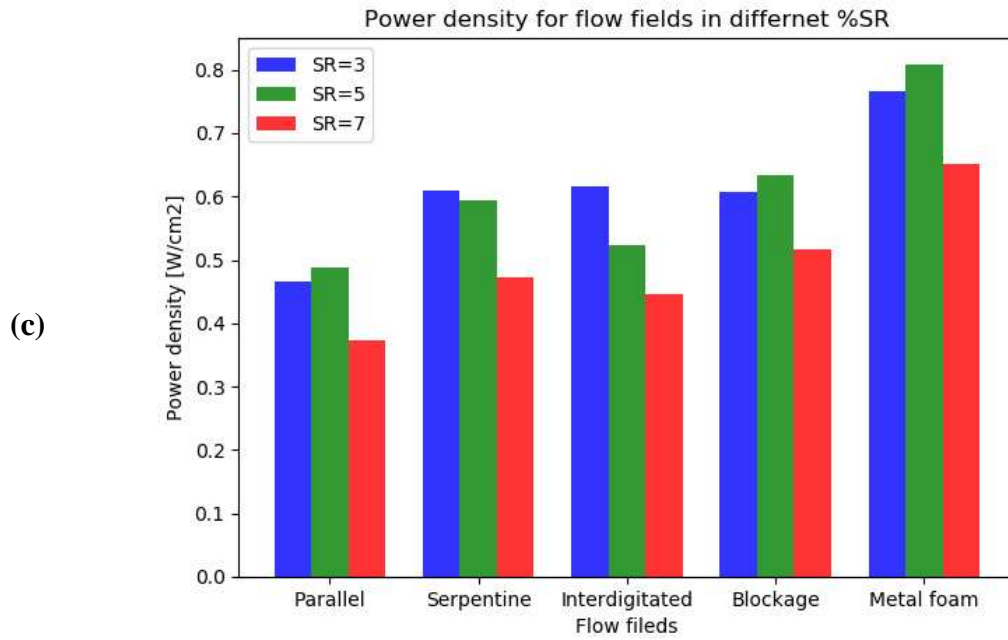


**Fig. 11.** Effect of stoichiometric ratio of cathodic flow for different flow field designs on (a) total pressure drop (Pa), (b) liquid water saturation and (c) power density ( $\text{W}/\text{cm}^2$ ).

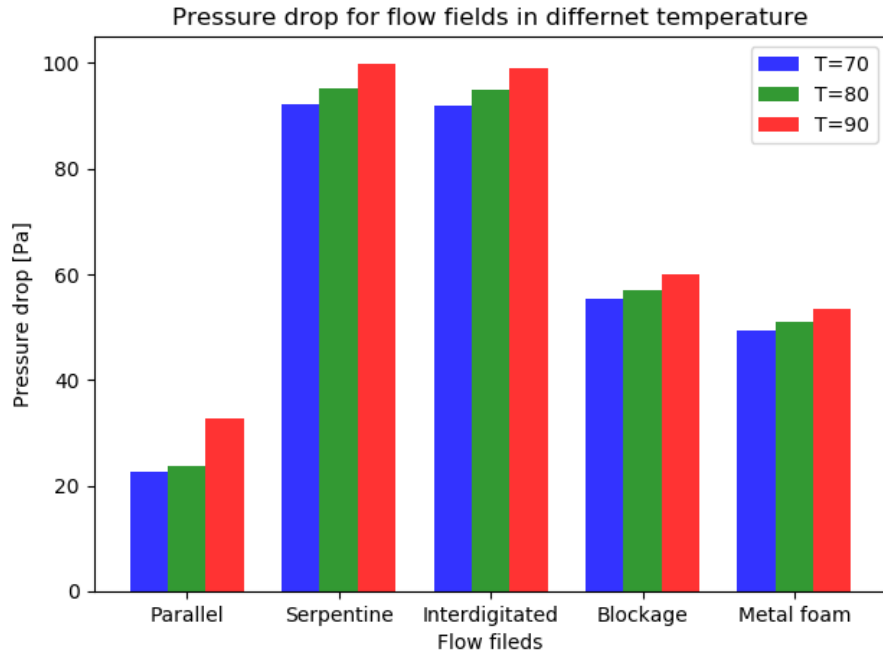
The effect of the stoichiometric ratio of the cathodic flow on the output power density for the various investigated flow fields is shown in Fig. 11 (c). It shows that, for the interdigitated and serpentine flow fields, the output power density decreases as the stoichiometric ratio increases. Corroborated with the corresponding liquid water saturations results shown in Fig. 11 (b), this is most likely due to the decreased amount of water available for membrane humidification. On the other hand, there exist optimum values for the stoichiometric ratio at which the power density is a maximum for the parallel, metal foam and partially blocked parallel flow fields; such optimum values appear to ensure an adequate supply of oxygen and water to the catalyst layer and the membrane electrolyte respectively. In comparison with Fig 10 (c), one could see that the power density is more sensitive to the cathodic relative humidity than to the stoichiometric ratio of the cathodic flow.

### 3.3.3. Effect of cathode inlet flow temperature

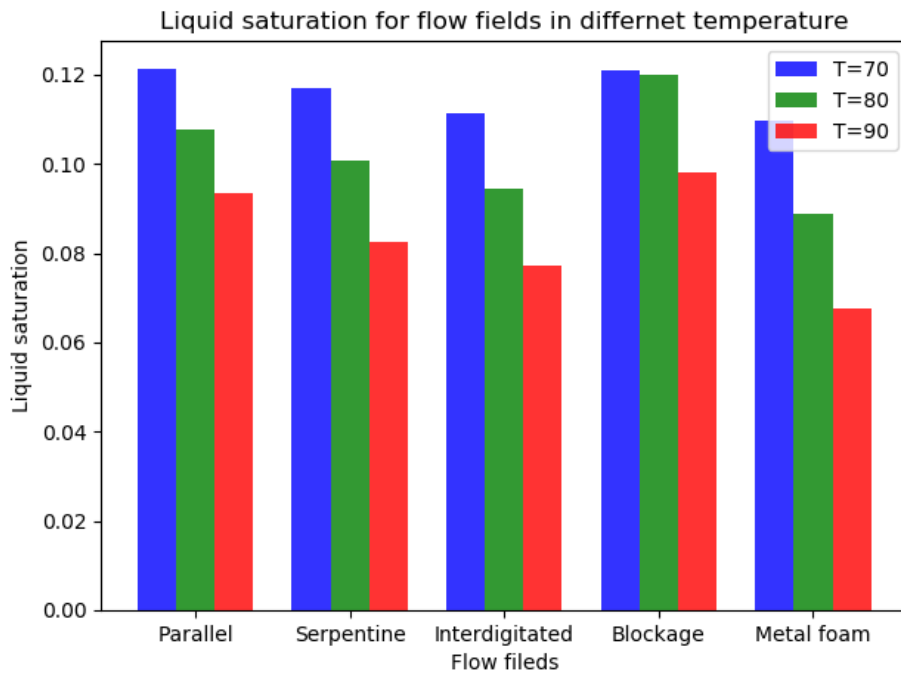
The impact of the temperature of the cathodic inflow on the pressure drop, liquid water saturation and power density for different flow field designs is displayed in Fig. 12. It can

be noted that, for all the investigated flow fields, the pressure drop slightly increases with increasing temperature and this is due to the fact that, as evidenced from ideal gas law, pressure increases with increasing temperature. Compared with Fig. 10 (a) and Fig. 11 (a), one could see that the pressure drop is slightly more sensitive to the temperature of the cathodic inflow than to the cathodic relative humidity; however, the pressure drop remains much more sensitive to the stoichiometric ratio of cathodic flow rate than to the temperature of the cathodic inflow. The computed pressure drop values are shown in Fig. 10(a), 11(a), 12(a), for the metal foam and partially-blocked flow fields show intermediate pressure drop, lies between the corresponding values of the parallel and the serpentine and interdigitated flow fields. The effect of the temperature of the cathodic inflow on the liquid water saturation in the CL for the investigated flow fields is presented in Fig. 12 (b). One could see from the figure that the liquid water saturation in general decreases as inflow temperature increases. Compared with Fig. 10 (b), the liquid water saturation increases with cathode relative humidity and decreases with a temperature of the cathodic inflow. When compared with Fig. 11 (b), the effect of both the stoichiometric ratio and the temperature on the liquid water saturation in the cathode CL is almost of the same magnitude for all the investigated flow designs; for the parallel case, as shown, the saturation is almost insensitive to the change in inflow temperature.

(a)



(b)



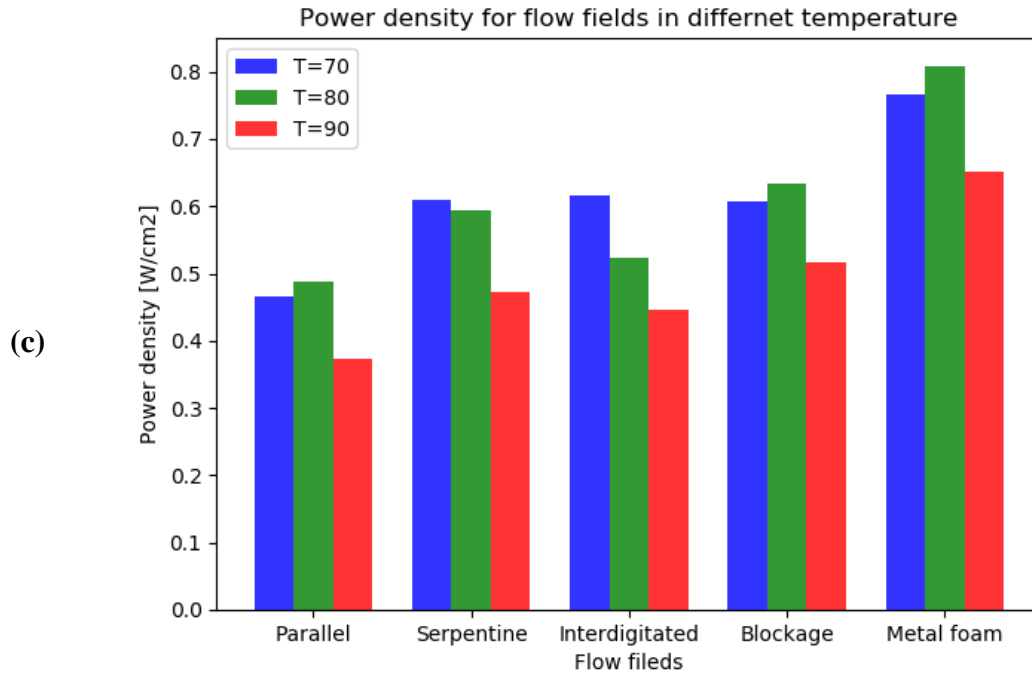


**Fig. 12.** Effect of temperature of cathode inlet flow for different flow distributors: (a) total pressure drop (Pa), (b) liquid saturation, and (c) power density ( $\text{W}/\text{cm}^2$ ).

Fig 12 (c) shows the effect of the temperature of the cathodic inflow on the output power density for the all investigated flow field designs. It can be seen from the figure that, for the employed set of temperatures, there exists an optimum value for the temperature of the cathodic inflow at which the output power density is a maximum for the parallel, partially blocked parallel and metal foam flow fields, i.e.  $80^\circ\text{C}$ . The optimum temperature can be resulted in due to the balance of decrease in the membrane conductivity and increase in the rate of reaction; as temperature rises, the membrane conductivity lowers, whereas the reaction kinetics improves. On the other hand, the last figure shows that the output power density decreases as the temperature of the cathodic inflow for the serpentine and interdigitated flow fields increases. Given the fuel cell operating conditions and MEA structure, it appears that the modeled fuel cell suffers from membrane dehydration and thus oxygen transport to the CL is not the controlling process. As such, an increase in the inflow humidity results in better membrane humidification and hence enhances the overall cell performance.

#### **4. Conclusions**

A multiphase three-dimensional CFD model of a PEMFC, which incorporates all the anisotropic properties of the GDL, was developed to investigate the influence of the cathode flow field design on the fuel cell performance. The investigated designs were five different flow field distributors: three conventional (single parallel, serpentine and interdigitated) and two recently-introduced ones (parallel with staggered blocks and porous metal foam). Upon validation of the developed model with the experimental data from the literature, a comprehensive comparison was performed in terms of the global performance and the distributions of the key variables. A parametric study was also conducted for all the investigated flow fields to evaluate the effects of the relative humidity, stoichiometric ratio, and temperature of the cathode inflow on the pressure drop, liquid water saturation, and output power density. Below are the main findings of the study:

- The best-simulated performance is presented by the fuel cell operating with the metal foam flow field; the peak power density, compared to that of the base parallel flow field case, increases by about 50%. This is attributed to the lowest liquid water saturation demonstrated by the metal foam flow field, decreasing the mass transport resistance and allowing more reactant gas, oxygen in this case, to reach the reactive sites in the catalyst layer. On the other hand, compared with that of the parallel flow fields, about a 10% increase in the peak power density is observed when using serpentine, interdigitated or partially-blocked parallel flow fields.
- The modeled fuel cell with the parallel and metal foam flow fields demonstrate the most uniform distribution of the current density and this is due to the relatively uniform distribution of oxygen concentration with these two flow fields. On the other hand, the serpentine and the interdigitated flow fields show the least uniform

distribution of the current density and oxygen concentration implying that they are more susceptible to hot spots.

- The lowest and most uniform distribution of water saturation was obtained when using the metal foam flow field and this is due to the presence of relatively strong convective flow. On the other hand, owing to the relatively poor convective flow, the modeled fuel cell with the parallel flow field shows the highest values of liquid water saturation. High values of water saturation were found to exist within the vicinity of the blocks for the modeled fuel cell with the parallel flow field with the staggered blocks and this is due to the presence of stagnant flows in the areas of the GDL beneath the blocks.
- The metal foam design generally maintains its superiority, as evidenced by its highest power density, over other designs as the relative humidity, stoichiometric ratio or the temperature of the cathodic inflow changes. Notably, the interdigitated flow field design outperforms other designs, including metal foam design, at low humidity conditions.
- Interestingly, there exist optimum values for the stoichiometric ratio (i.e. 5) and the temperature (i.e. 80°C) of the cathode inflow at which the performance gain of the parallel, metal foam and partially-blocked flow fields is maximized.

**Nomenclature:**

PEMF	proton exchange membrane fuel cell	UDS	user defined scalar
C	gas diffusion layer	FVM	finite volume method
GDL	catalyst layer	AMG	algebraic multi grid
CL	computational fluid dynamics		
CFD	membrane electrode assembly		
MEA	proton exchange membrane	<b>Greek</b>	
PEM	source/sink rate	<b>symbols</b>	
S	velocity, $m\ s^{-1}$		
u	diffusivity, $m^2\ s^{-1}$		
D	liquid water saturation	$\rho$	liquid density, $kg\ m^3$
		$\mu$	dynamic viscosity, Pa.s

s	temperature, K	$\varepsilon$	porosity
T	pressure, Pa	$\omega$	species mass fraction
P	exponent for the pore blockage	$\varnothing_s$	solid phase potential, V
n	diffusivity of the species i	$\varnothing_m$	membrane phase potential, V
$D_i$	characteristics pore length of the catalyst	$\sigma$	electrical conductivity, S m <sup>-1</sup>
$r_p$	molecular weight of the species i, Kg mol <sup>-1</sup>	$\alpha_a$	anode transfer coefficient
$M_i$		$\alpha_c$	cathode transfer coefficient
R	universal gas constant, J mol <sup>-1</sup> K <sup>-1</sup>	$\zeta$	specific active surface area, m <sup>-1</sup>
HOR	hydrogen oxidation reaction	$\eta_{act}$	activation overpotential, V
ORR	oxygen reduction reaction	$\lambda$	water content
F	Faraday constant, C mol <sup>-1</sup>	$\theta$	contact angle of GDL
C	molar concentration, mol m <sup>-3</sup>	$\theta_a$	stoichiometric flow ratio at anode
$j_a$	exchange current density at anode, A m <sup>-3</sup>	$\theta_c$	stoichiometric flow ratio at cathode
$j_c$	exchange current density at cathode, A m <sup>-3</sup>		
$U^\circ$	equilibrium potential, V	<b>Subscripts</b>	
$n_d$	electro-osmotic drag coefficient	g	gas
EW	equivalent weight of Nafion, Kg mol <sup>-1</sup>	k	species
$y_w$	local water mole fraction	ref	reference
k	permeability, m <sup>2</sup>	a	anode
$k_0$	absolute permeability, m <sup>2</sup>	c	cathode
$p_c$	capillary pressure, Pa	Naf	Nafion
J (s)	Leverett function	equal	equilibrium
$C_p$	heat capacity of the gas mixture, J kg <sup>-1</sup> K <sup>-1</sup>	w	water
$k_T$		l	liquid
xx, zz	thermal conductivity, W m <sup>-1</sup> K <sup>-1</sup>	s	solid
yy	vector direction in the in-plane	f	fluid
$h_{fg}$	vector direction in through-plane	act	activation
$A_{pore}$	latent heat of water, J kg <sup>-1</sup>	con	condensation
$Sh_c$	pore surface per volume	eva	evaporation
$Sh_e$	transfer rate coefficient for condensation	ohm	ohmic
i	transfer rate coefficient for evaporation	rev	reversible
$r_a$	current density, A m <sup>-2</sup>	<b>Superscripts</b>	
$r_c$	rate coefficient of membrane for absorption	eff	effective quantity
$A_{ch}$	rate coefficient of membrane for desorption	K	Knudsen diffusivity, m <sup>2</sup> s <sup>-1</sup>
$A_m$		m	membrane
x			
UDF	cross-sectional area of the gas channel		
	active surface area of the membrane		
	species mole fraction		
	user-defined function		

## References

- [1] Jung C, Shim H, Koo S, Lee S, Yi S. Investigations of the temperature distribution in proton exchange membrane fuel cells. *Appl Energy*. 2012;93:733-741. doi:10.1016/j.apenergy.2011.08.035.
- [2] El-kharouf A, Chandan A, Hattenberger M, Pollet BG. Proton exchange membrane fuel cell degradation and testing: review. *J Energy Inst*. 2012;85(4):188-200. doi:10.1179/1743967112Z.00000000036.
- [3] Ji M, Wei Z. A Review of Water Management in Polymer Electrolyte Membrane Fuel Cells. *Energies*. 2009;2(4):1057-1106. doi:10.3390/en20401057.
- [4] Qin C, Rensink D, Fell S, Majid Hassanizadeh S. Two-phase flow modeling for the cathode side of a polymer electrolyte fuel cell. *J Power Sources*. 2012;197:136-144. doi:10.1016/j.jpowsour.2011.08.095.
- [5] Cao T-F, Lin H, Chen L, He Y-L, Tao W-Q. Numerical investigation of the coupled water and thermal management in PEM fuel cell. *Appl Energy*. 2013;112:1115-1125. doi:10.1016/j.apenergy.2013.02.031.
- [6] Afshari E, Mosharaf-Dehkordi M, Rajabian H. An investigation of the PEM fuel cells performance with partially restricted cathode flow channels and metal foam as a flow distributor. *Energy*. November 2016:1-11. doi:10.1016/j.energy.2016.10.101.
- [7] Kahraman H, Orhan MF. Flow field bipolar plates in a proton exchange membrane fuel cell: Analysis & modeling. *Energy Convers Manag*. November 2016. doi:10.1016/j.enconman.2016.10.053.

- [8] Lim BH, Majlan EH, Daud WRW, Husaini T, Rosli MI. Effects of flow field design on water management and reactant distribution in PEMFC: a review. *Ionics (Kiel)*. 2016;22(3):301-316. doi:10.1007/s11581-016-1644-y.
- [9] Li X, Sabir I. Review of bipolar plates in PEM fuel cells: Flow-field designs. *Int J Hydrogen Energy*. 2005;30(4):359-371. doi:10.1016/j.ijhydene.2004.09.019.
- [10] Wang J. Theory and practice of flow field designs for fuel cell scaling-up: A critical review. *Appl Energy*. 2015;157:640-663. doi:10.1016/j.apenergy.2015.01.032.
- [11] Manso AP, Marzo FF, Barranco J, Garikano X, Garmendia Mujika M. Influence of geometric parameters of the flow fields on the performance of a PEM fuel cell. A review. *Int J Hydrogen Energy*. 2012;37(20):15256-15287. doi:10.1016/j.ijhydene.2012.07.076.
- [12] Chiu H, Jang J, Yan W, Li H, Liao C. A three-dimensional modeling of transport phenomena of proton exchange membrane fuel cells with various flow fields. *Appl Energy*. 2012;96:359-370.
- [13] Kerkoub Y, Benzaoui A, Haddad F, Ziari YK. Channel to rib width ratio influence with various flow field designs on performance of PEM fuel cell. *Energy Convers Manag*. 2018;174(May):260-275. doi:10.1016/j.enconman.2018.08.041.
- [14] Limjeerajarus N, Charoen-Amornkitt P. Effect of different flow field designs and number of channels on performance of a small PEFC. *Int J Hydrogen Energy*. 2015;40(22):7144-7158. doi:10.1016/j.ijhydene.2015.04.007.
- [15] Lee B, Park K, Kim H. Numerical Optimization of Flow Field Pattern by Mass Transfer and Electrochemical Reaction Characteristics in Proton Exchange Membrane Fuel Cells. *Int J Electrochem Sci*. 2013;8:219-234.
- [16] Lim BH, Majlan EH, Daud WRW, Rosli MI, Husaini T. Numerical analysis of

- modified parallel flow field designs for fuel cells. *Int J Hydrogen Energy*. 2017;42(14):9210-9218. doi:10.1016/j.ijhydene.2016.03.189.
- [17] Freire LS, Antolini E, Linardi M, Santiago EI, Passos RR. Influence of operational parameters on the performance of PEMFCs with serpentine flow field channels having different (rectangular and trapezoidal) cross-section shape. *Int J Hydrogen Energy*. 2014;39(23):12052-12060. doi:10.1016/j.ijhydene.2014.06.041.
- [18] Roshandel R, Arbabi F, Moghaddam GK. Simulation of an innovative flow-field design based on a bio inspired pattern for PEM fuel cells. *Renew Energy*. 2012;41:86-95. doi:10.1016/j.renene.2011.10.008.
- [19] Kloess JP, Wang X, Liu J, Shi Z, Guessous L. Investigation of bio-inspired flow channel designs for bipolar plates in proton exchange membrane fuel cells. *J Power Sources*. 2009;188(1):132-140. doi:10.1016/j.jpowsour.2008.11.123.
- [20] NG. V. US Patent No. 5,981,098, 1999. 1999.
- [21] JK. N. US Patent No. 5,776,624, 1998.
- [22] Tsai B-T, Tseng C-J, Liu Z-S, et al. Effects of flow field design on the performance of a PEM fuel cell with metal foam as the flow distributor. *Int J Hydrogen Energy*. 2012;37(17):13060-13066. doi:10.1016/j.ijhydene.2012.05.008.
- [23] Tseng C-J, Tsai BT, Liu Z-S, Cheng T-C, Chang W-C, Lo S-K. A PEM fuel cell with metal foam as flow distributor. *Energy Convers Manag*. 2012;62:14-21. doi:10.1016/j.enconman.2012.03.018.
- [24] Heidary H, Kermani MJ. Performance enhancement of fuel cells using bipolar plate duct indentations. *Int J Hydrog Energy*. 38(13):5485-5496.
- [25] Heidary H, Kermani MJ, Prasad AK, Advani SG, Dabir B. Numerical modelling of in-line and staggered blockages in parallel flowfield channels of PEM fuel cells. *Int J Hydrogen Energy*. November 2016:1-13.

- doi:10.1016/j.ijhydene.2016.10.076.
- [26] Tiss F, Chouikh R, Guizani a. A numerical investigation of reactant transport in a PEM fuel cell with partially blocked gas channels. *Energy Convers Manag.* 2014;80:32-38. doi:10.1016/j.enconman.2013.12.063.
- [27] Tseng C-J, Heush Y-J, Chiang C-J, Lee Y-H, Lee K-R. Application of metal foams to high temperature PEM fuel cells. *Int J Hydrogen Energy.* 2016;41(36):16196-16204. doi:10.1016/j.ijhydene.2016.06.149.
- [28] Carton JG, Olabi a. G. Three-dimensional proton exchange membrane fuel cell model: Comparison of double channel and open pore cellular foam flow plates. *Energy.* February 2016. doi:10.1016/j.energy.2016.02.010.
- [29] Yuan W, Tang Y, Yang X, Wan Z. Porous metal materials for polymer electrolyte membrane fuel cells – A review. *Appl Energy.* 2012;94:309-329. doi:10.1016/j.apenergy.2012.01.073.
- [30] Afshari E, Ziaei-Rad M, Shariati Z. A study on using metal foam as coolant fluid distributor in the polymer electrolyte membrane fuel cell. *Int J Hydrogen Energy.* 2016;41(3):1902-1912. doi:10.1016/j.ijhydene.2015.10.122.
- [31] Afshari E, Baharlou Houreh N. Performance analysis of a membrane humidifier containing porous metal foam as flow distributor in a PEM fuel cell system. *Energy Convers Manag.* 2014;88:612-621. doi:10.1016/j.enconman.2014.08.067.
- [32] Pasaogullari U, Mukherjee PP, Wang C-Y, Chen KS. Anisotropic Heat and Water Transport in a PEFC Cathode Gas Diffusion Layer. *J Electrochem Soc.* 2007;154(8):B823. doi:10.1149/1.2745714.
- [33] Nguyen PT, Berning T, Djilali N. Computational model of a PEM fuel cell with serpentine gas flow channels. *J Power Sources.* 2004;130(1-2):149-157. doi:10.1016/j.jpowsour.2003.12.027.

- [34] Bernardi DM, Verbrugge MW. A Mathematical Model of the Solid-Polymer-Electrolyte Fuel Cell. *J Electrochem Soc.* 1992;139(9):2477. doi:10.1149/1.2221251.
- [35] Khandelwal M, Mench MM. Direct measurement of through-plane thermal conductivity and contact resistance in fuel cell materials. *J Power Sources.* 2006;161(2):1106-1115. doi:10.1016/j.jpowsour.2006.06.092.
- [36] Meng H, Wang C-Y. Electron Transport in PEFCs. *J Electrochem Soc.* 2004;151(3):A358. doi:10.1149/1.1641036.
- [37] Wu H, Li X, Berg P. On the modeling of water transport in polymer electrolyte membrane fuel cells. *Electrochim Acta.* 2009;54(27):6913-6927. doi:10.1016/j.electacta.2009.06.070.
- [38] Cheng CH, Lin HH, Lai GJ. Numerical prediction of the effect of catalyst layer Nafion loading on the performance of PEM fuel cells. *J Power Sources.* 2007;164(2):730-741. doi:10.1016/j.jpowsour.2006.11.039.
- [39] Springer TE, Zawodzinski T a., Gottesfeld S. Polymer electrolyte fuel cell model. *J Electrochem Soc.* 1991;138(8):2334-2342. doi:10.1149/1.2085971.
- [40] Tomadakis MM, Sotirchos S V. Ordinary and Transition Regime Diffusion in Random Fiber Structures. 1993;39(3):397-412.
- [41] Iranzo A, Muñoz M, Rosa F, Pino J. Numerical model for the performance prediction of a PEM fuel cell. Model results and experimental validation. *Int J Hydrogen Energy.* 2010;35(20):11533-11550. doi:10.1016/j.ijhydene.2010.04.129.
- [42] Rashapov R, Imami F, Gostick JT. A method for measuring in-plane effective diffusivity in thin porous media. *Int J Heat Mass Transf.* 2015;85:367-374. doi:10.1016/j.ijheatmasstransfer.2015.01.101.

- [43] Barbir F, Barbir F. Chapter Four – Main Cell Components, Material Properties, and Processes. In: PEM Fuel Cells. ; 2013:73-117. doi:10.1016/B978-0-12-387710-9.00004-7.
- [44] Ismail MS, Hughes KJ, Ingham DB, Ma L, Pourkashanian M. Effects of anisotropic permeability and electrical conductivity of gas diffusion layers on the performance of proton exchange membrane fuel cells. 2012;95:50-63. doi:10.1016/j.apenergy.2012.02.003.
- [45] Yang X-G, Ye Q, Cheng P. Hydrogen pumping effect induced by fuel starvation in a single cell of a PEM fuel cell stack at galvanostatic operation. Int J Hydrogen Energy. 2012;37(19):14439-14453. doi:10.1016/j.ijhydene.2012.07.011.
- [46] Wang Y, Wang C. A Nonisothermal, Two-Phase Model for Polymer Electrolyte Fuel Cells. J Electrochem Soc. 2006;153(6):1193-1200. doi:10.1149/1.2193403.
- [47] Dagan G. Flow and Transport in Porous Formations. Berlin: Springer-Verlag; 1989.
- [48] Wu H, Berg P, Li X. Steady and unsteady 3D non-isothermal modeling of PEM fuel cells with the effect of non-equilibrium phase transfer. Appl Energy. 2010;87(9):2778-2784. doi:10.1016/j.apenergy.2009.06.024.
- [49] He W, Yi JS, Van Nguyen T. Two-phase flow model of the cathode of PEM fuel cells using interdigitated flow fields. AIChE J. 2000;46(10):2053-2064. doi:10.1002/aic.690461016.
- [50] Arvay a., Ahmed a., Peng X-H, Kannan a. M. Convergence criteria establishment for 3D simulation of proton exchange membrane fuel cell. Int J Hydrogen Energy. 2012;37(3):2482-2489. doi:10.1016/j.ijhydene.2011.11.005.
- [51] Esfeh HK, Azarafza A, Hamid MKA. On the computational fluid dynamics of PEM fuel cells (PEMFCs): An investigation on mesh independence analysis. RSC

Adv. 2017;7(52):32893-32902. doi:10.1039/c7ra03236f.

- [52] Wang L. A parametric study of PEM fuel cell performances. Int J Hydrogen Energy. 2003;28(11):1263-1272. doi:10.1016/S0360-3199(02)00284-7.

**{Bibliography}**